UNIVERSITY OF OKLAHOMA

GRADUATE COLLEGE

ANALYSIS OF FLOW AND THERMODYNAMIC CHARACTERISTICS AT A SITE IN COMPLEX TERRAIN

A THESIS

SUBMITTED TO THE GRADUATE FACULTY

in partial fulfillment of the requirements for the

Degree of

MASTER OF SCIENCE IN METEOROLOGY

By

TYLER M. BELL
Norman, Oklahoma
2018

Downloaded from SHAREOK. Persistent Handle URL: https://hdl.handle.net/11244/301327

ANALYSIS OF FLOW AND THERMODYNAMIC CHARACTERISTICS AT A SITE IN COMPLEX TERRAIN

A THESIS APPROVED FOR THE
SCHOOL OF METEOROLOGY

BY

Dr. Petra Klein, Chair

Dr. Chris Fiebrich

Dr. Scott Salesky

© Copyright by TYLER M. BELL 2018
All Rights Reserved.

Acknowledgments

I would like to first thank my advisor, Petra Klein, for giving me the opportunity to work on this project. It has been a wonderful growing experience for me and has made a lasting impact. Additionally, I would like to thank Chris Fiebrich and Scott Salesky for being willing to serve on my committee.

I would like to extend my gratitude to Norman Wildmann and Robert Menke for both providing data and giving constructive criticism as I worked through the project, as well as being great friends.

Many thanks to my office mates Elizabeth Smith, Josh Gebauer, Eric Loken, and Brian Greene for creating a spectacular working environment full of collaboration and hypothetical field experiments. Also thanks to Matt Carney for being a good friend and trusting me to help work on the CLAMPS reconfiguration with him.

I would be remiss if I did not thank the people of Portugal for allowing us to take over Vale do Cobrao for a couple months and collect such an interesting dataset.

Finally, I would like to thank Katie Bell for her support and love through this experience.

Table of Contents

Acknowledgments **iv**

List of Tables **viii**

List of Figures **ix**

Abstract **xiv**

1 Introduction and Background **1**

1.1 Past work on Complex Terrain 2

1.2 Recent Experiments 9

1.3 The New European Wind Atlas 10

1.3.1 Perdigão Experiment 11

1.3.2 Layout of Instrumentation Network 13

2 OU Instrumentation **15**

2.1 The Collaborative Lower Atmospheric Mobile Profiling System . . . 15

2.1.1 CLAMPS Reconfiguration 16

2.2 CLAMPS Data Processing 17

2.2.1 AERI 17

2.2.2 Microwave Radiometer 19

2.2.3 Doppler Lidar 19

2.2.4 Realtime Data Processing 22

3 Perdigão Flow Characteristics **25**

3.1 Local Wind Characteristics 25

3.2 Thermodynamic Characteristics 27

3.3 Case Study Selection 30

3.3.1 May 22-23, 2017 32

3.3.2 May 7-8, 2017 33

3.3.3 May 20-21, 2017 33

3.3.4 May 21-22, 2017 34

4 Virtual Tower Analysis **41**

4.1 Doppler Lidars 41

4.1.1 OU DL 41

4.1.2 The German Aerospace Center (DLR) DLs 42

4.1.3 DTU DLs 42

4.1.4 Virtual Towers 43

4.2 Methods 44

4.2.1 Uncertainty Analysis 45

4.3 Results 47

4.3.1 Sensitivity of Uncertainty to Elevation 47

4.3.2 Comparison of Wind Retrieval Techniques 50

4.3.3 Spatial Analysis 52

4.3.3.1 Case 1 53

4.3.3.2 Case 2 54

5 Concluding Remarks and Future Work **60**

5.1 Conclusions 60

5.2 Future Work 61

Bibliography **62**

List of Tables

3.1 Table outlining the number of days where particular phenomena were observed using the CLAMPS system. 32

4.1 Characteristics of the RHI scans performed by each DL in Perdigão. 42

List of Figures

1.1 Elevation (m) and layout of meteorological towers within the valley. Three transects were parallel to the ridges: one along the SW ridge (denoted riSW_01-riSW_08), one in the valley (denoted vall_01-vall_07), and one on the NE ridge (denoted riNE_01-riNE_07). Additionally, two transects were perpendicular to the ridges: one NW of the turbine (denoted trNW_01-trNW_16) and one SE of the turbine (denoted trSE_01-trSE_15). The Lower Orange site was a highly utilized site during the IOP where to observe flows throughout the valley due to its centralized location and proximity to the wind turbine. 14

2.1 CLAMPS in a) its mobile configuration and b) in the new configuration that was designed for Perdigão. 17

2.2 RMS Error calculated from the two versions of the AERI retrievals taking the collocated radiosondes to be truth. 18

2.3 Time (UTC) height plot from 12 UTC on May 23, 2017 to 12 UTC on May 24, 2017 of a) V1 potential temperature retrievals from the AERI at 5 minute intervals, b) wind speed from the CLAMPS DL VAD scan in 15 minute intervals, c) wind direction from the CLAMPS DL VAD scan, d) 15 minute averages of vertical velocity from the CLAMPS DL stare, and e) σ_w from the averages. The dashed line is the height of the base of the wind turbine on the southwest ridge, which is used as a proxy for ridge height. 23

2.4 Example cross-valley (a) and along-valley (b) RHI scans from CLAMPS on May 24, 2017. The RHI is projected in such a way that positive values are winds in the +x direction and vice versa. The vectors in the center are the winds from the closest VAD projected into the same plane as the RHI. The wind barbs to the right are from the VAD in ms^{-1}. In a), the +x direction points to the NE, while in b), the +x direction points in the NW direction. 24

3.1 Wind roses computed using the CLAMPS DL data collected from 06 UTC to 20 UTC. These times encompass the daytime hours during the campaign. The four heights show flow characteristics well within the valley (70 m), near ridge top (240 m), and in the middle of the boundary layer. 26

3.2 Same as Fig. 3.1 but for data collected during the nighttime hours (20 UTC to 06 UTC). 27

3.3 Time series of all CLAMPS DL VAD wind speed and wind direction data at two levels, one level near ridge height and one level close to the background wind level discussed in Section 3.1. The x-axis is relative to 00 UTC (e.g. -2 would be 22 UTC). Colors are based on the average wind direction near ridge height from 0 to 6 UTC during a given night with red being north-easterly and blue being south-westerly. 28

3.4 Timeseries of a) surface potential temperature and b) $\frac{d\theta}{dz}$ calculated from the surface to approximately ridge height using version 1 of the AERI data. The x-axis is relative to 00 UTC (e.g. -2 would be 22 UTC). Colors are based on the average wind direction near ridge height from 0 to 6 UTC during a given night with red being north-easterly and blue being south-westerly. 29

3.5 Same as Figure 3.4, but the red color now represents nights where the average $\frac{d\theta}{dz}$ was greater than .01 K/m from 0 to 6 UTC. 30

3.6 Same as Figure 3.3, but the red color now represents nights where the average $\frac{d\theta}{dz}$ was greater than .01 K/m from 0 to 6 UTC. 31

3.7 Same as Figure 2.4, except for 22 UTC on May 22, 2017. 35

3.8 Same as Figure 2.3, except for the time period from 12Z May 22nd to 12Z on May 23rd. 36

3.9 Same as Figure 2.3, except for May 7th at 00 UTC to May 8th at 12 UTC. The AERI retrival in a) is a special 5-minute time resolution from the V2 dataset. Note the strong, shallow inversion in the valley and the weak wind overnight on the 8th, while the winds on the night of the 7th are much stronger and the potential temperature profile is more well mixed. 37

3.10 Same as Figure 2.3, except for May 20st at 12 UTC to May 21nd at 12 UTC. 38
3.11 Same as Figure 2.3, except for May 21st at 12 UTC to May 22nd at 12 UTC. 39
3.12 Same as figure 3.7a, except for May 22, 2017 during the period of turbulence above ridge height. Notice how flow over the ridge at -900 m appeared smooth while flow at approximately 600 m appeared turbulent as it went over the ridge. 40

4.1 Map of DLs, meteorological towers, and virtual towers at the Perdigão site. 43
4.2 Uncertainties of the virtual towers associated with the locations of the DLs. 48
4.3 Depiction of the setup used to test the sensitivity of the uncertainty in the 3D tower to the elevation angle of the CLAMPS DL. 49
4.4 Results of the the uncertainty analysis for R=300 and H=200 with $\epsilon_r = .2ms^{-1}$. Vertical dotted lines are locations of virtual towers. The x axis is normalized by the height of the point being observed. 50
4.5 Profiles from each of the different wind estimation techniques. Note the height axis is relative to the base of the wind turbine. In general, the methods agree well above the ridge, but results are inconsistent 100 m below ridge height. Tower data is still preliminary. 51

4.6 Top: Along valley cross section of the flow from the early morning of May 7th at 03 UTC. The color fill is the LOS velocity projected into the horizontal from the OU RHI used to create the virtual towers. Positive values indicate flow in the +X direction, which is directed to the NW. The overlaid vectors are the components of the virtual towers projected into the plane of the RHI scan. The inset plot shows how the terrain cross sections are oriented. The dashed line indicates the ridge top and the solid lines correspond to the terrain cross section from the inset plot. Bottom row: Similar to the top row, only in the cross valley sense. +X here points to the NE. . . . 56

4.7 Same as Figure 4.6, but for the morning of May 8th around 0230 UTC. 57

4.8 Same as Figure 4.6, but for the morning of May 8th around 05 UTC. 58

4.9 Same as Figure 4.6, but for May 23rd. Additionally, plot on the bottom are all 2D retrievals because DLR85 was not operating correctly. WS5 is missing for the same reason. 59

Abstract

The goal of the Perdigão Field Experiment was to study atmospheric flows in complex terrain and to collect a high-quality dataset for the validation of meso- and micro-scale models. An Intensive Observation Period (IOP) was conducted from May 1, 2017 through June 15, 2017 where a multitude of instruments was deployed in and around two nearly parallel, 5 km long ridges separated by a 1.4 km wide valley perpendicular to the prevalent wind directions in the region. During this IOP, the Collaborative Lower Atmospheric Mobile Profiling System (CLAMPS) was deployed and operated in the valley between the ridges. The CLAMPS facility, which was developed as a joint effort between the School of Meteorology at OU and NOAA's National Severe Storms Laboratory (NSSL), utilizes a microwave radiometer (MWR), an atmospheric emitted radiance interferometer (AERI), and a scanning Doppler lidar (DL) to profile the boundary layer with a high temporal and spatial resolution. Optimized DL scanning strategies and joint retrievals for the MWR and AERI data provide detailed information about the wind, turbulence and thermodynamic structure from the surface up to 1000 m AGL on most nights; profiles can extend higher depending on aerosol concentrations and cloud cover. Over the course of the IOP, CLAMPS observed many different phenomena. During some nights, with stronger prevailing winds that were directed perpendicular to the valley, waves were observed at the ridges and in the valley. At the same time, radiational cooling led to katabatic flows in the valley, particularly during nights when synoptic scale forcing was weak.

In addition to CLAMPS, the Technical University of Denmark (DTU) operated eight Leosphere Windcube 200S scanning DLs and the German Aerospace Center (DLR) contributed three DLs of the same kind to capture flow features above the ridges and in the valley. The arrangement of DLs presented an opportunity to retrieve four virtual towers every 15 minutes where Range Height Indicator (RHI) scans of individual instruments intersected. The virtual towers typically encompassed heights from 50 m to 600 m above the valley floor, extending the range of traditional in-situ observations located throughout the valley. Additionally, they provide data in low altitude areas where other DL processing techniques (such as Velocity Azimuth Displays or Doppler Beam Swinging scans) may have trouble retrieving accurate wind speeds due to the high spatial flow variability and prevalence of significant vertical motions in complex terrain. Along with the wind speed and direction, uncertainties associated with the DLs were propagated through the retrieval. A few case studies will be presented to highlight the usefulness of these virtual towers.

Chapter 1

Introduction and Background

The planetary boundary layer (PBL) is unequivocally the most important layer of the atmosphere to Earth's ecosystems. It is the layer affected by the exchange processes with the surface. The momentum, heat, and mass exchanges within the PBL are highly affected by the characteristics of the land surface and terrain. Large-scale features of the terrain, the land use, and other forcings can modify the surface fluxes and lead to complex flow patterns in the PBL, which can be important to the transport of water vapor in the hydrological cycle or the transport of trace gases, including pollutants that are harmful to humans.

Dispersion models, wind power models, numerical weather prediction models, and climate models all depend on a detailed understanding of these fluxes to accurately predict the future state of the atmosphere. Current PBL frameworks (e.g., Monin-Obukhov similarity theory) are based on the assumption of homogeneous terrain, and thus break down in complex terrain. However, models still use these frameworks since there is no suitable alternative. These downfalls are especially prevalent in the wind energy sector.

As renewable energy becomes more desirable, more turbines will need to be erected, and it will be crucial to site these turbines in areas that maximize their output. Of particular interest these days is the siting of wind turbines in complex terrain. As early as the 1940s, Putnam (1948) recognized the promise of siting

wind turbines on the top of hills to take advantage of the speedup that occurs as air flows over the hill. It will also be critical for power companies to be able to forecast how much power will be produced in the short term (on the scale of days). Annually, a 1% error in wind speed could result in billions in revenue lost by energy companies (Banta et al., 2013). The understanding of flow in complex terrain is of value to a variety of other sectors as well.

1.1 Past work on Complex Terrain

As would be expected, much of the initial theoretical basis for the boundary layer was based on flat, homogeneous terrain to reduce the degrees of freedom and thus the difficulty in predicting the kinematics and thermodynamics. Monin and Obukhov (1959) worked to determine some basic laws of turbulent mixing in the surface layer (where fluxes are assumed to be constant with height) that were vital to many works that followed. Willis and Deardorff (1974) were pioneers in developing similarity theory of the convective mixed layer, again for flat, homogeneous terrain. This came out of initial attempts to model turbulence through large eddy simulation (LES) by Deardorff (1972, 1974).

The first forays into the study of more complex flows that accounted for terrain concentrated on micro-meteorological flows encountering a step change in surface roughness. Elliott (1958) was the first to introduce a theory for the internal boundary layer that forms downwind of a step change in surface roughness. In the years following, Taylor (1962) and Panofsky and Townsend (1964) also developed theories attempting to describe how the internal boundary layer grows after a step change in surface roughness.

Around this same time, some of the first experimental studies were also being done. One such experiment involved introducing a roughness element change by lining up Christmas trees on a frozen lake (Stearns, 1964; Kutzbach, 1961)

and measuring modifications to wind speed and temperature in the surface layer downstream of the roughness change. In a later, more controlled experiment, a wire mesh on a flat runway was used to investigate and evaluate some differences between Elliot's theory and the Panofsky-Townsend theory (Bradley, 1968). However, as Bradley (1968) points out in his discussion,

> "most natural surfaces are notably irregular, both as regards shape, size, and distribution of the roughness elements, and there is much to be said for a parameter which integrates the effects of all elements in the flow above them."

While the step change in surface roughness helped understand flow over terrain on the microscale, these studies still assumed flat terrain and horizontally homogeneous winds. Jackson and Hunt (1975) (hereafter JH75) were one of the first to identify the need to analytically study near surface flow in complex terrain. Specifically, JH75 addressed the turbulent boundary layer over a low hill since previous work only looked at laminar flow over a gentle hill (Smith, 1973; Hunt, 1971). JH75 split the flow into two regions and solved the equations of motion for each layer separately. They specified an inner layer of height l where turbulent exchange processes affect the flow, and a region at a sufficiently high height such that it is essentially inviscid.

JH75 defined a characteristic length scale, L, to be "the horizontal distance from the top of the hill to the point at which the height is half the maximum height" and the height of the hill is designated as h. The hill was assumed to be small and shallow ($h/L << 1$) and have a constant surface roughness length (z_0) to linearize the equations. The equation for l in JH75 is:

$$\frac{l}{L}\ln(\frac{l}{z_0}) = 2\kappa^2 \tag{1.1}$$

where κ is the von Karman constant and z_0 is the roughness length. In the outer region, the pressure perturbations associated with the hill created symmetric winds over the hill. In the inner region, the wind speed maximum over the crest of the hill is located at the boundary with the outer layer. The maximum wind speed in the wake of the hill is contained inside the inner layer. JH75 found their model fit qualitatively well to the limited observations and experiments available at that time.

In the years following the publication of this theory, much progress was made in evaluating flow over complex terrain. Theoretically, there were numerous expansions made to JH75. For example, Mason and Sykes (1979) generalized the theory to three-dimensional (3D) hills and Sykes clarified some assumptions made in JH75 (Sykes, 1980). Hunt et al. (1988) also expanded the theory to be able to handle a multitude of different upwind wind profiles. In the JH75 original theory, perturbation velocities in the two layers were defined differently (since they were in different layers with different dynamical properties). Therefore, equations were solved separately for each layer, causing a discontinuity at the interface between them. Hunt et al. (1988) matched up the wind profiles in the inner and outer layer by introducing a third, intermediate layer. Experiments testing JH75 show that the theory incorrectly identified the location of the wind speed maximum at the crest of the hill (Bradley, 1980; Mason and King, 1985; Britter et al., 1981), so Hunt et al. (1988) addressed this shortfall as well.

There were many field experiments conducted following JH75. One of the most famous field experiments to examine the "rules of thumb" (such as locations of maximum wind speed under different upwind conditions) that had emerged from some of the theories of flow over a shallow hill was the Askervein Hill experiment in the United Kingdom (Taylor and Teunissen, 1987). This site was chosen because it was moderately shallow, uniform, and suitable for numerical modeling even though

it was asymmetric. Many in-situ instruments were deployed in transects across the hill to record wind speed and direction, temperature, humidity, precipitation, and pressure. Mickle et al. (1988) set out in part to determine whether the JH75 or the Jensen et al. (1984) definition for l was more accurate. Jensen et al. (1984) predicted l to behave as:

$$\frac{l}{L}\ln^2(\frac{l}{z_0}) = 2\kappa^2 \tag{1.2}$$

This relation produces smaller values for l. Further studies showed that the Jensen et al. (1984) formula tended to produce values of l closer to observed values (Taylor et al., 1987; Taylor and Teunissen, 1987). All these studies questioned whether l should be considered a level where something specific occurs (e.g., wind speed max at the crest like in JH75), or whether it could be considered only an order of magnitude constant (Teunissen et al., 1987) or a scale height for the inner layer (Taylor et al., 1987). Claussen (1988) noted that JH75 had derived a more general equation for l,

$$\frac{l}{L}\ln(\frac{l}{z_0}) = c \tag{1.3}$$

where c depends on the type of closure assumption used. JH75 used the mixing-length closure and ended up with $c = 2\kappa^2$. However, since this was a general relation, c could be fitted to data and a universal constant might be found. Walmsley et al. (1986) found that the Claussen formula agreed better with the Askervein observations, where L/z_0 was small. However, the Claussen equation was calibrated using values of L/z_0 similar to the Askervein Hill (Taylor and Teunissen, 1987), so naturally it would perform better.

The data from the Askervein Hill experiment were and continue to be used to evaluate linear and non-linear models developed to handle flow in terrain. There is considerable interest in making simple models that are fit for commercial use,

and the linear theory in JH75 and its extensions proved very useful in this regard. There were a series of linear models developed based on the work of JH75 (Walmsley et al., 1986). Additionally, Beljaars et al. (1987) created a Mixed Spectral Finite-Difference Model. However, while these models did reasonably well in predicting the acceleration of winds cresting the Askervein Hill (albeit with a slight overestimation), they did not perform well in the lee of the hill, where they overestimated wind speeds. Teunissen et al. (1987) note that this could be caused by slight flow separation, in which case non-linear effects could not be ignored. Kim and Patel (2000) noted that this could have been caused by the hills in the surrounding area. When they ran their Reynolds Averaged Navier-Stokes (RANS) model with the surrounding terrain included, they noted flow separation in the lee of Askervein. However, by excluding the surrounding terrain, no flow separation was observed. They note that many earlier experiments neglected the surrounding terrain and that could explain why linear theory did not match with observations.

Thus far, only neutrally stratified flows have been considered. Stratification has a great effect on flows over terrain. Hunt et al. (1988) extended JH75 to allow stable stratification. They also introduced a four-layer model to account for problems with boundary conditions in JH75.

In a stably stratified flow, flow can become stagnated on the upwind side of a hill and end up going around the sides of a hill if the kinetic energy from the mean wind can not overcome the potential energy required to lift a parcel through the stable density gradient. An important parameter in stratified flow over terrain is the Froude Number,

$$F = U_0(H)/NH \tag{1.4}$$

where U_0 is the characteristic velocity at a characteristic height H and N is the Brunt-Vaisala frequency defined as

$$N = \sqrt{\frac{g}{\theta_0}\frac{d\theta}{dz}} \tag{1.5}$$

where g is the gravitational acceleration, θ is the potential temperature, θ_0 is a reference potential temperature, and z is height. F is the ratio of inertia forces to gravity forces (Arya, 2001). For $F << 1$ (very stable stratification), studies show that flows approaching a 3D hill will have some parcels close to the ground flowing around the hill while parcels higher up can flow over the hill. This means there must be some streamline which divides the level of parcels that makes it over the hill and parcels that go around the hill. This is called the dividing streamline. Sheppard (1956) suggested, based on energy arguments, that the height of the dividing streamline (for stratified approach flow with a constant density gradient) is $H_s = H(1 - F)$. Lab experiments concluded that this was a useful equation for finding the dividing streamline height (Snyder et al., 1985). The experiments also found that the width-to-height ratio of the hill did not make a large difference in H_s, but high aspect ratios could cause blocking upstream of the hill. Leo et al. (2016) extended Sheppard's relation by introducing a logarithmic profile for the upwind speed in F. The theory was tested in The Mountain Terrain Atmospheric Modeling and Observations Program (MATERHORN; Fernando et al., 2015), but there was not enough quality data collected to reach any conclusions about the success of the new formula. However, the one case they had looked promising.

Stratified flows can also lead to the formation of waves in the lee of a disturbance. Work in the 1930s and 1940s provided the framework for more advanced analytical solutions of mountain waves (see Queney (1948) for a technical review). Scorer (1949) derived an analytical solution to trapped lee waves and sparked a slew of research into mountain meteorology (Scorer and Wilkinson, 1956; Sawyer, 1962). As Wood (2000) notes, this period of intense work on the subject was likely

due to a combination of the need to understand mountain flows for flight considerations, an interest in wind energy applications, and the invention of the computer and numerical weather prediction. Research on the topic picked up rapidly once JH75 was introduced and researchers started expanding it as discussed above.

While all of the analytical work discussed so far has been based on linear theory, non-linear effects of terrain have been studied extensively as well. There are many different types of non-linear flows possible over complex terrain. One of the most basic non-linear effects is flow separation. This occurs when vorticity generated on the lee side of the slope produces a reverse flow near the surface. When this reverse flow meets the downslope flow, there is a region of convergence at the surface which lifts the streamline away from the slope, creating two separate flows (Wood, 1995). Wood worked to study the onset of flow separation by finding a critical slope angle where flow separation occurs based on linear analysis. Results from his study show that the critical angle is approximately twice what it was thought to be before. Ayotte and Hughes (2004) used wind tunnel studies to investigate this flow separation to determine how to approach how to account for flow separation. They suggest that the turbulence time and length scales in the lee of the hill scale based on the length of the hill as opposed to the height above the surface like the upwind side. Another non-linear phenomena is the acceleration of winds down the lee-side slope followed by a hydraulic jump. These are often referred to Chinook winds and are caused by a high speed flow capped by an elevated inversion (Arya, 2001).

Terrain can also induce its own flows even if no background flow is present. Katabatic flows were first analytically described by Prandtl (1942) for a stably stratified fluid along a uniformly cooled, sloping surface. The original theory has been extended numerous times (Egger, 1985; Shapiro and Fedorovich, 2007, 2008, and many others). Since katabatic flows occur along a cooled surface, they are

stably stratified and vertical mixing as well as the depth of the flow is limited. Pollutants tend to pool in cold pools associated with katabatic flow and can be harmful to humans (Fernando, 2010).

1.2 Recent Experiments

Many experiments in recent years have set out to collect data to further the understanding of ABLs in complex terrain. As mentioned earlier, MATERHORN took place in 2012 to study a variety of different terrain effects (Fernando et al., 2015) on ABL flow.

Grachev et al. (2016) studied the structure of turbulence in katabatic flows overnight using meteorological towers placed on the slope. Katabatic flows have a speed maximum just above the surface. They found that in a slope following coordinate system, the signs of momentum fluxes reversed depending on whether or not they were below or above the speed maximum. Using this, they propose a method to estimate the height of the speed maximum using linear interpolation. They also found that turbulence above the speed maximum is completely decoupled from the surface.

Complex terrain does now always refer to hill/mountainous terrain, but can be simply heterogeneity of the land surface and subsurface. Jensen et al. (2016) examined near surface fluxes at two different sites during the MATERHORN campaigns, specifically they studied how counter-gradient heat fluxes varied between the two sites during the early evening transition. They found considerable differences in the evolution and timing of counter-gradient fluxes, largely due to underlying thermal characteristics of the soil.

Another large experiment was the Terrain Induced Rotor Experiment (T- REX) (Grubišić et al., 2008). This experiment set out to intensively study rotors created by lee waves at a high spatio-temporal resolution in the Sierra Nevada region. The

experiment collected a large amount of data and the experiment was considered a great success. Flow was found to be highly three-dimensional within the lee of the mountains. Under quiescent conditions, multiple distinct layers of flow characteristics were observed associated with terrain flows. Additionally, many different Doppler lidar techniques were tested. Weissmann et al. (2009) made vorticity calculations with line-of-sight velocities, Drechsel et al. (2009) used a variational technique commonly used for radars to derive three-dimensional wind vector from two Doppler lidars, and Hill et al. (2010) used co-planar lidar scans to analyze how rotors propagated throughout the valley.

There is still much to learn about flows in complex terrain. Dynamics on all scales and their interactions are still not fully understood. Additionally, no scaling laws (like MOST in flat terrain) have been discovered for complex terrain. For example, wind turbine wakes are very small scale phenomena, but they can have huge impacts on other turbines in a wind farm. These wakes can also modify fluxes in the environment which could be felt at larger scales. However, the magnitude of the wakes are uncertain in complex terrain, whereas they are well characterized in flat terrain (Calaf et al., 2010, 2011). Turbulence as a whole is still poorly understood in complex terrain. The scientific community is increasingly using LES to study problems like this, but the models still need work, especially in complex terrain. To develop new scaling laws, develop new ABL parameterizations, and validate the models using these new parameterizations, more and more high spatio-temporal datasets in complex terrain will be needed.

1.3 The New European Wind Atlas

As wind energy becomes more popular, the need for models to accurately predict energy output from wind resources becomes increasingly important. Due to this need, the European Union funded a large project called the New European Wind

Atlas (Mann et al., 2017). The goal of NEWA is to provide a standardized dataset of wind energy resources for Europe through the creation of new and improved meso- and micro-scale models and modeling techniques. One important aspect of developing these modeling techniques is to verify their accuracy next to a high quality dataset. Therefore, one of the main goals in the creation of the NEWA is to develop new verification methodologies and then assess them based on large scale measurement campaigns. To do this, multiple field experiments were designed to cover a range of different types of flows and land cover (e.g., forested hills, complex terrain, offshore, etc).

1.3.1 Perdigão Experiment

During the spring and early summer of 2017, a field experiment took place in Central Portugal to study complex terrain. Participants planned to look at wind turbine wake characteristics in complex terrain, the effect of the terrain on the approach flow, dynamical processes underlying the diurnal cycle, the effect of topographic heterogeneity on the flows in predominantly 2D topography, fluxes due to thermally driven flows, and improvement of lidar processing techniques and deployment strategies, just to name a few.

Another goal is the generation of another high quality dataset akin to the Askervein dataset for validation of meso- and micro-scale models. To validate microscale models, detailed measurements of the flow at multiple scales are required. As has already been mentioned, data collected from the Askervein Hill project in 1982 (Taylor and Teunissen, 1987) are still a standard used to evaluate how well models handle flow over complex terrain. The experiments taking place under the NEWA are meant to augment the measurements from Askervein while adding another layer of complexity.

The Perdigão Experiment is one of the multiple measurement campaigns that took place for NEWA. Perdigão is a small municipality located in central Portugal that sits adjacent to two parallel ridges of nearly equal height separated by a valley with steep slopes called Vale do Cobrão. The ridge axes extend northwest to southeast and are approximately 1.4 km apart. It was thought that two parallel ridges is the best approximation in nature to study flow over periodic, sinusoidal terrain.

Additionally, there was a single 2 MW wind turbine located on the southwest ridge. Wind resources are significantly affected by terrain and land cover. For example, winds at hub height are much higher at the top of a hill than they are on the lee side of the hill. Flows on the lee side of the hill, depending on the stability conditions, wind speeds, etc., can behave in multiple different ways, all of which are important when determining sites where wind turbines will consistently be able to produce energy.

Leading up to the Intensive Observation Period (IOP) in the Spring of 2017, a meteorological tower had been operating on the SW ridge for many years. Data from 2002-2004 were used to construct a climatology of the wind directions over the ridge. According to the climatology, winds often were found to be directed perpendicular to the two ridges (Vasiljević et al., 2017). This provided an opportunity to see how flow behaved going over the ridges. To gather the desired observations, a multi-national group of scientists from Europe and the United States converged in Perdigão to measure complex flow at unprecedented spatio-temporal scales. A combination of meteorological towers, DLs, radiometers, and other in-situ platforms were dispersed throughout the valley.

1.3.2 Layout of Instrumentation Network

Similar to the Askervein study, meteorological towers equipped with sonic anemometers, temperature, and humidity sensors were used to record data at multiple heights in different transects of the valley. There were three transects aligned parallel to the valley (one on each ridge crest and one in the valley) as well as two cross-valley transects (Figure 1.1). Tower heights ranged from 10 to 100 m. Additionally, 42 remote sensors were dispersed throughout the valley including 28 scanning Doppler lidars (DLs) that were set up to measure the flow entering, within, and exiting the valley. Some DLs were sited in such a way that they could be combined into multi-Doppler retrievals throughout the valley and in the wake of the wind turbine. Three Microwave Radiometers were also set up inside and outside of the valley so that thermodynamic characteristics of the flow could be measured as it enters and leaves the valley.

The goal of this thesis is to provide an initial analysis of the conditions during the Intensive Observation Period (IOP), from May 1, 2017 through June 15, 2017, as observed by instrumentation from OU and answer questions including the following:

1. What were the climatological conditions during the IOP and how did they compare to the climatology performed before the IOP?

2. Are there any clear patterns that arise as a result of stability, wind speed, wind directions, etc.? How often were certain phenomena observed during the campaign and under what conditions did we see these phenomena?

3. Given the abundance of DLs in the experiment, can combinations of these DLs into multi-Doppler retrievals help augment more traditional measurement method in complex terrain, such as in situ measurements and single DL wind retrievals?

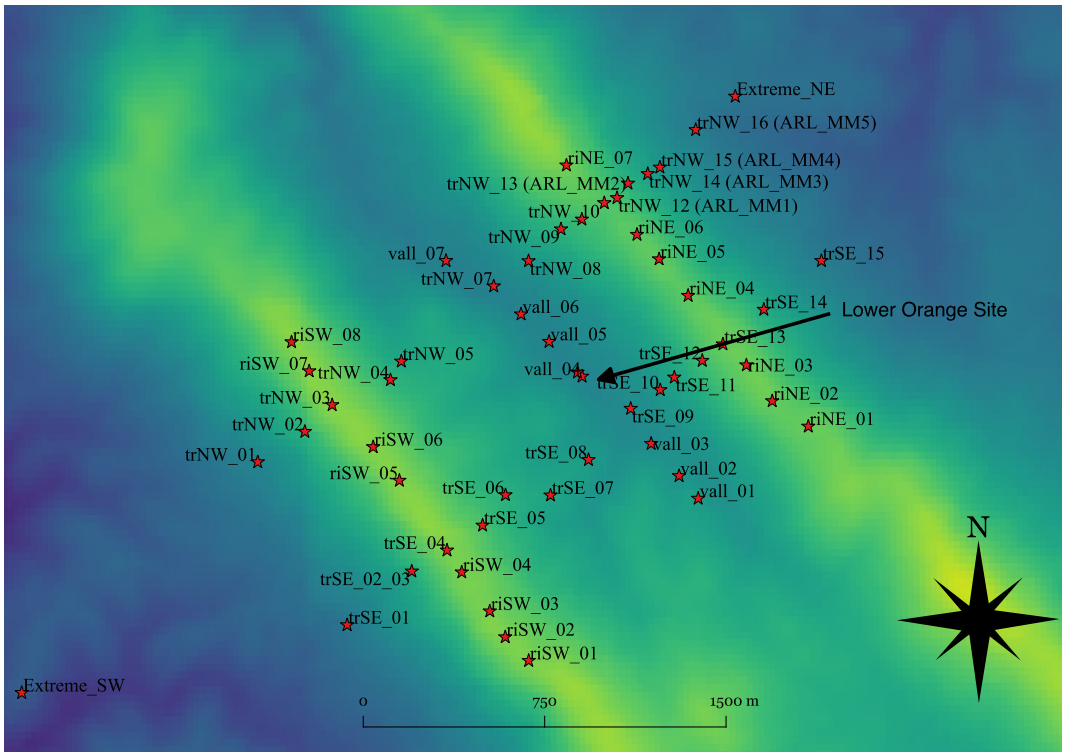

Figure 1.1: Elevation (m) and layout of meteorological towers within the valley. Three transects were parallel to the ridges: one along the SW ridge (denoted riSW_01-riSW_08), one in the valley (denoted vall_01-vall_07), and one on the NE ridge (denoted riNE_01-riNE_07). Additionally, two transects were perpendicular to the ridges: one NW of the turbine (denoted trNW_01-trNW_16) and one SE of the turbine (denoted trSE_01-trSE_15). The Lower Orange site was a highly utilized site during the IOP where to observe flows throughout the valley due to its centralized location and proximity to the wind turbine.

Chapter 2

OU Instrumentation

2.1 The Collaborative Lower Atmospheric Mobile Profiling System

The University of Oklahoma (OU) deployed the Collaborative Lower Atmospheric Mobile Profiling System (CLAMPS) at the lower Orange site (named due to the presence of an orange grove in the adjacent field) located inside the valley during the IOP (Figure 1.1). CLAMPS includes a Halo Photonics Scanning DL that performed both cross- (NE to SW) and along-valley (NW to SE) range height indicator (RHI) scans every 15 minutes using 2.5 degree steps in elevation. In addition, a 24 point, 70 degree plan position indicator (PPI) scan was performed every 15 minutes proceeding the RHIs. A PPI scan gives a representation of the spatial variability in the horizontal by scanning at a fixed elevation and only moving in azimuth, while a RHI scan essentially takes a cross section of the flow by staying at a fixed azimuth, but changing elevation. The remainder of the time, the DL was in vertical stare mode to gather vertical velocity statistics.

CLAMPS also utilizes an Atmospheric Emitted Radiance Interferometer (AERI, Knuteson et al., 2004a,b) to retrieve thermodynamic profiles of the atmosphere.

The AERI measures downwelling radiation in the infrared spectrum at a high spectral resolution between the wavelengths of 3.3 and 19.2 μm. It has two blackbody targets, one at a fixed temperature and one at ambient temperature, to help maintain its calibration. A downwelling spectrum can be measured roughly every 30 s.

CLAMPS also utilizes a Humidity and Temperature Profiling (HATPRO) Microwave Radiometer (Rose et al., 2005) for boundary layer temperature and humidity profiling. Similar to the AERI, it measures downwelling radiation from the atmosphere, but does so in the microwave spectrum. The HATPRO measures radiation in 14 different channels distributed over various absorption lines. The HATPRO is able to make observations in all channels simultaneously, so that the temporal resolution is approximately 1 s. Since the addition of off-zenith elevation angles can also significantly improve retrievals, off-zenith angles were used during the IOP.

Using the AERI and MWR in a joint retrieval helps get more accurate profiles of the atmosphere. The AERI excels at retrieving low level gradients in temperature and moisture, while the MWR can get better retrievals at higher altitudes.

2.1.1 CLAMPS Reconfiguration

CLAMPS is usually integrated into a trailer to make it highly mobile and positionable (Figure 2.1a). Additionally, this configuration allows real time data processing and provides insight into flow phenomenon as it happens. However, the bulky trailer was not viable to ship overseas. Each instrument in the system is able to run standalone without the protection of the trailer, so it was decided to run them this way in Perdigão. However, data collection and processing would still be useful for other groups in the valley for deciding when to deploy certain instruments. Due to this, a custom trailer, smaller than the normal trailer, was

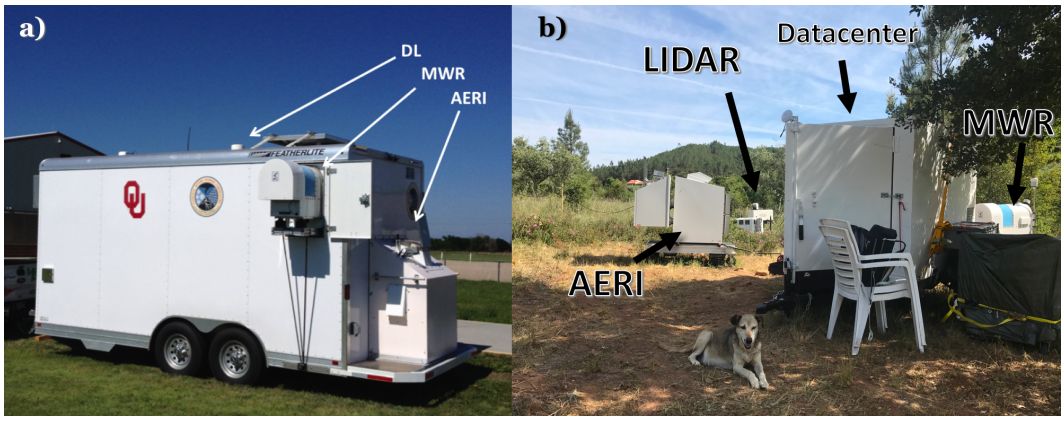

Figure 2.1: CLAMPS in a) its mobile configuration and b) in the new configuration that was designed for Perdigão.

built to house only the data system and all the hardware required to run the individual instruments in their standalone mode (Figure 2.1b). This configuration was simpler to ship overseas in a shipping container and still allowed real-time data to be viewed in the field.

2.2 CLAMPS Data Processing

2.2.1 AERI

AERI profiles were retrieved using the AERI Optimal Estimation (AERIoe) retrieval developed by Turner and Löhnert (2014). A first retrieval with a 10 minute averaging window was performed to get a version one (V1) dataset in real time so the resulting thermodynamic retrievals could be used to make decisions on when to perform additional operations, such as extra soundings and flying the University of Colorado (CU) tethered lifting system (TLS). Since the retrieval could have multiple solutions, an a priori dataset is needed to contrain the solution. The prior dataset used for the retrieval algorithm was derived from a database of radiosondes from Lisbon, Portugal. Though Lisbon was on the coast, and Perdigão far inland,

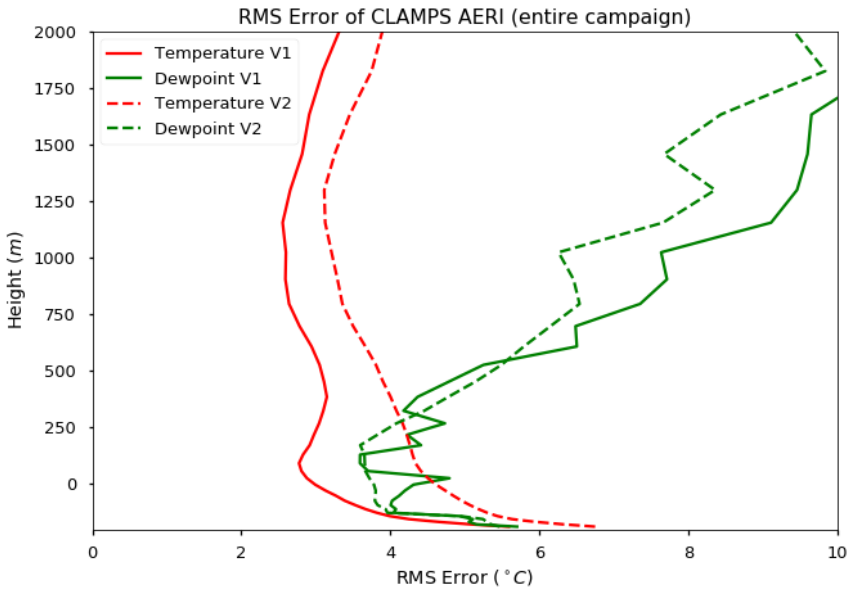

Figure 2.2: RMS Error calculated from the two versions of the AERI retrievals taking the collocated radiosondes to be truth.

temperatures from the first retrieval were acceptable at low levels when compared to the collocated radiosondes. Retrievals of water vapor did not perform well, likely due to the prior dataset being from a coastal atmosphere.

Post-IOP, the retrieval was run again to produce a version two dataset (V2) using the radiosondes released during the campaign to help constrain the upper levels. This ended up improving the retrievals in the upper levels, but made the retrievals slightly worse in the low levels. This is evident in Figure 2.2, which shows the root mean square (RMS) error from the two retrievals compared to the radiosondes released during the IOP. The RMS error profile from the V1 profile has lower RMS error than V2 up to 2 km above the surface. For all the work presented here, the V1 dataset will be used since the main focus area will be below 2 km in depth. Water vapor profiles will not be considered in the following chapters.

2.2.2 Microwave Radiometer

The MWR data from CLAMPS was processed using the MWR Optimal Estimation (MWRoe) retrieval described in Blumberg et al. (2015). The method is nearly identical to AERIoe and the same a priori dataset was used for both retrievals. MWRs must be calibrated often with liquid nitrogen as they are subject to radiometric drift, so a rigorous bias correction was performed to limit error in the retrievals.

First, clear sky periods were selected by calculating the standard deviation of the 31.4 GHz channel, which is sensitive to cloud cover, over one-hour windows centered on radiosonde launch times during the campaign. A strict threshold of .13 K was chosen; if the standard deviation for this time period was greater than the threshold, it was not used. The Monochromatic Radiative Transfer Model (MonoRTM) was used to convert the radiosonde data to radiances at the same bands the MWR measures for direct comparison. By doing this for all the bands during all the clear sky periods, a bias can be calculated for each band and fed into MWRoe.

Unfortunately, the initial MWRoe retrievals did not resolve any low level inversions in temperature, and therefore could not be trusted to give accurate measures of near surface stability. Improving these retrievals by including the off-zenith scans will be the subject of future work described in Chapter 5.

2.2.3 Doppler Lidar

DL systems have proven to be useful for many applications. They have been used for boundary layer meteorology (Klein et al., 2015; Fernando et al., 2015), wind energy research (Banta et al., 2015; Newman et al., 2016; Choukulkar et al., 2017), and other various fields of study. DLs measure the radial velocity along a beam

at high spatial and temporal resolution. Different scanning strategies can give different insights into the flow field surrounding the DLs.

By applying assumptions to the flow, one can use these different scan strategies to derive the two-dimensional (2D) and three-dimensional (3D) velocity vector from a single DL. The simplest techniques to derive the wind speed and direction are the velocity azimuth display (VAD) technique (Browning and Wexler, 1968) and the Doppler beam swinging (DBS) technique (Strauch et al., 1984). However, these techniques make the assumption that the wind is horizontally homogeneous in order retrieve the wind speed and direction; this is often not the case in boundary layer meteorology and can introduce errors into the wind retrievals. One area where the assumption of horizontal homogeneity is likely invalid is in the study of complex terrain, where atmospheric flows can have large spatial heterogeneity, which in turn, can introduce error and uncertainty into traditional retrievals (Bingöl et al., 2009; Bradley et al., 2015). Other techniques using a single DL have been developed to limit this assumption (Waldteufel and Corbin, 1979; Wang et al., 2015).

While retrieving the 3-D wind field from a single DL requires some potentially invalid assumptions, this can be solved by using multiple DLs with beams that intersect in the same area of space. By combining multiple different radial wind vectors, one can solve the 3D transformation matrix to get the 3D wind vector without assuming horizontal homogeneity. There are multiple configurations in which this can be done. For example, co-planar RHI scans were used in the Terrain-induced Rotor Experiment to study rotors caused by mountains (Hill et al., 2010), co-planar PPI scans were used in the Perdigão 2015 experiment to measure wind turbine wake deficits in highly complex terrain (Menke et al., 2018), and virtual towers were used in the Joint Urban Experiment in 2003 (Calhoun et al., 2006).

Multi-Doppler measurements can augment more traditional observation strategies and are highly adaptable to an experiment's science objectives. Though some

accuracy is lost due to volumetric averaging, the results are still quite accurate (Damian et al., 2014; Debnath et al., 2017). However, higher levels of uncertainty have been found when using more complicated scan strategies (Choukulkar et al., 2017) and under unstable conditions (Newman et al., 2016).

As part of the quality assurance checks on the CLAMPS DL, an intensity threshold of 1.01 was applied to all DL data. Intensity is calculated by simply adding 1 to the signal-to-noise ratio. Päschke et al. (2015) recommended a slightly more conservative threshold of 1.015, but this removed too much data during periods of lower intensity. Additionally, the first two range gates are disregarded in all calculations since they are prone to errors due to the characteristics of the DL laser. VADs were calculated from the PPI scans using a least-squares fitting of the radial velocities as a function of azimuth to the radial velocity equation:

$$V_r(\theta) = u \sin\theta \cos\phi + v \cos\theta \cos\phi + w \sin\phi \tag{2.1}$$

where ϕ is the elevation, θ is the azimuth, and u (east-west), v (north-south), and w (vertical) are the wind components in the traditional meteorological sense. The VADs were combined with the RHI scans to get a sense of how the flow moved over the ridges. This is expanded upon in Chapter 3. Additionally, the RHI scans were combined with RHIs from other participants in the IOP to derive virtual towers throughout the valley. This is discussed in Chapter 4.

Vertical velocity variance was calculated from the vertical stare data collected, however there has not been any quality control or corrections made to account for system noise in these measurements. Work is being done to use and improve upon the method described in Lenschow et al. (2000) to get a better estimate of the true variance. However, good measurements of vertical velocity variance can still be obtained if the signal-to-noise ratio is high (Bonin et al., 2016), and for the most part this is the case during the IOP.

2.2.4 Realtime Data Processing

To assist in making decisions in the field, scripts were developed to process data from CLAMPS and upload it to a web database. At least once a day (or whenever necessary), scripts downloaded DL and V1 AERI data from the processing system and produced plots similar to those in Figures 2.3 and 2.4. Though the vertical stares were captured at 1 s resolution, they were averaged to 15 minute intervals so vertical velocity statistics (i.e. variance) could be calculated to get a sense of how turbulent flow in and above the valley were. VADs have 15 minute time resolution and 28 m height resolution.

Figures similar to Figure 2.3 can be found at `http://weather.ou.edu/~tybell/clamps/` while animations of figures similar to Figure 2.4 can be found at `http://weather.ou.edu/~tybell/perdigao_rhi/`.

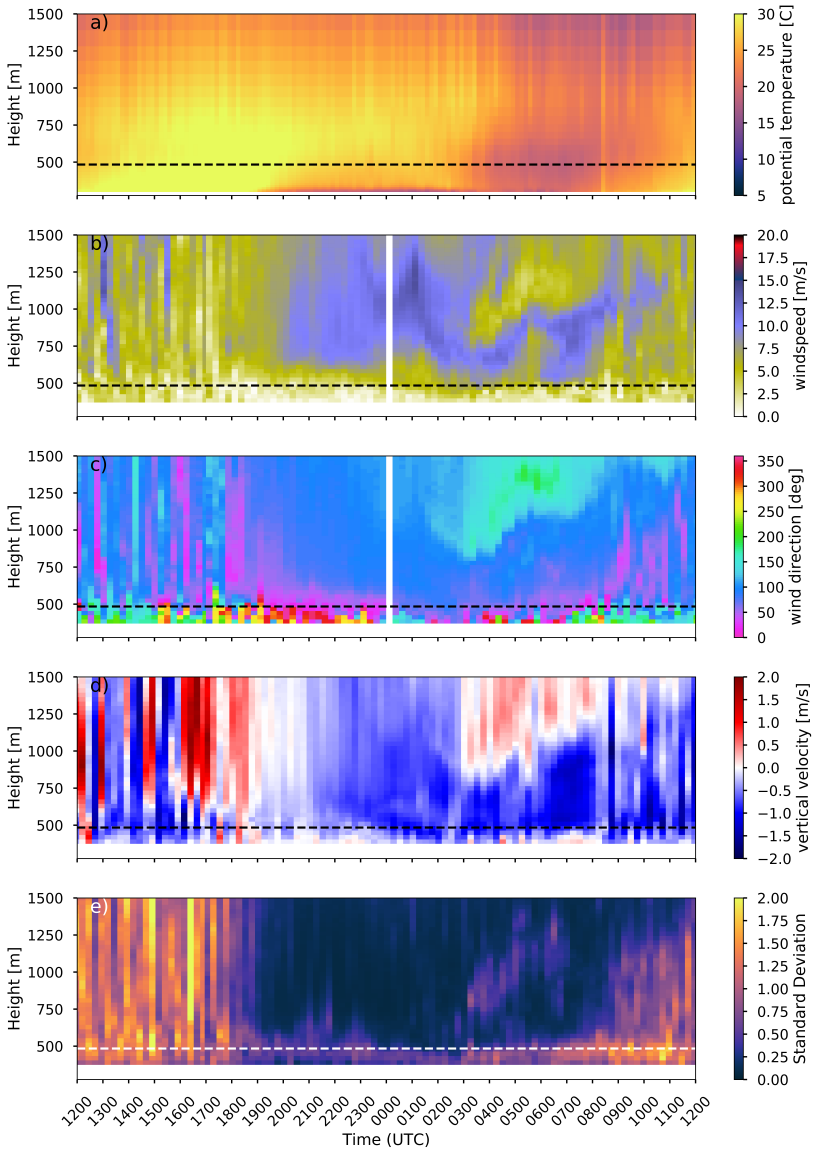

Figure 2.3: Time (UTC) height plot from 12 UTC on May 23, 2017 to 12 UTC on May 24, 2017 of a) V1 potential temperature retrievals from the AERI at 5 minute intervals, b) wind speed from the CLAMPS DL VAD scan in 15 minute intervals, c) wind direction from the CLAMPS DL VAD scan, d) 15 minute averages of vertical velocity from the CLAMPS DL stare, and e) σ_w from the averages. The dashed line is the height of the base of the wind turbine on the southwest ridge, which is used as a proxy for ridge height.

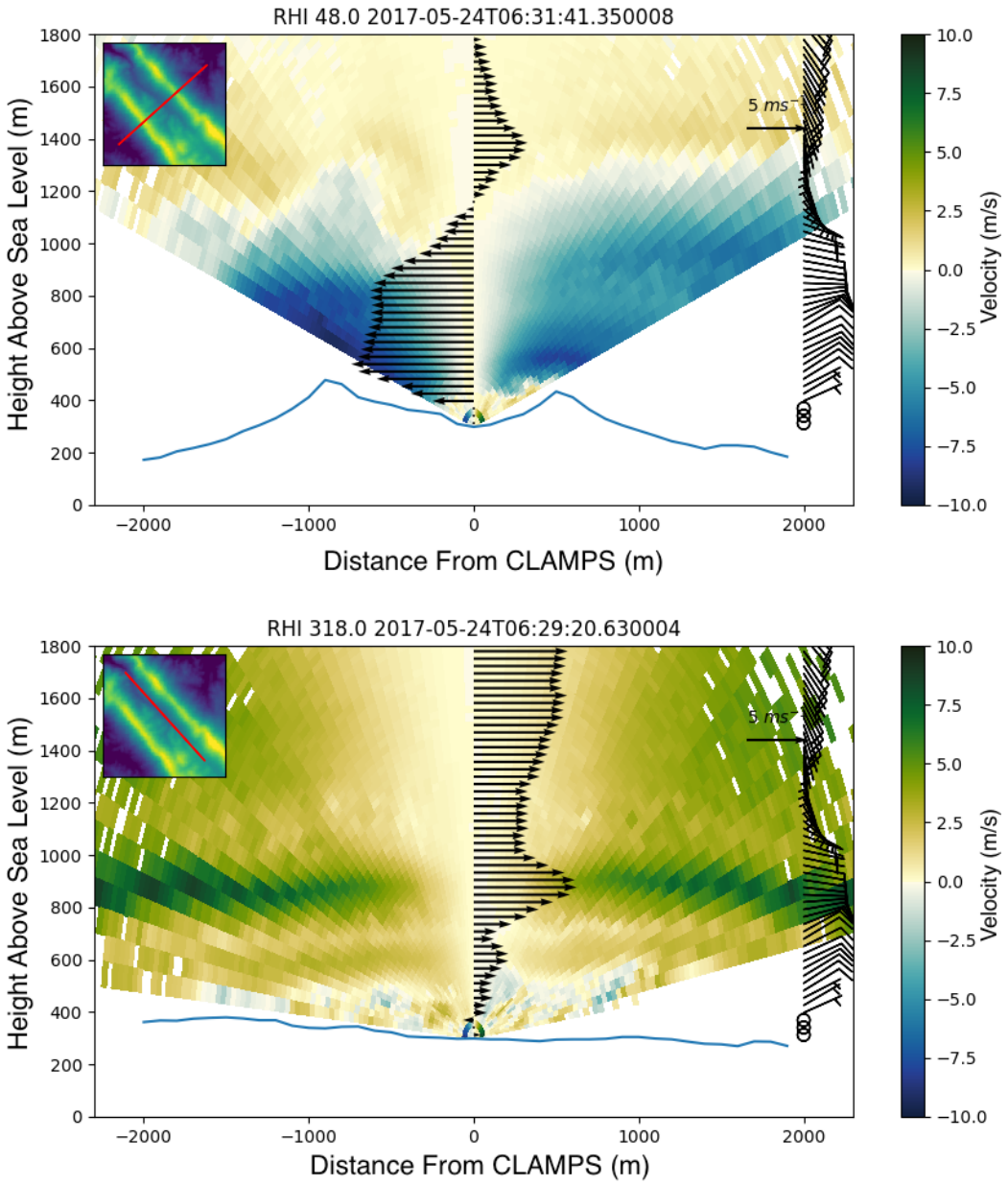

Figure 2.4: Example cross-valley (a) and along-valley (b) RHI scans from CLAMPS on May 24, 2017. The RHI is projected in such a way that positive values are winds in the +x direction and vice versa. The vectors in the center are the winds from the closest VAD projected into the same plane as the RHI. The wind barbs to the right are from the VAD in ms^{-1}. In a), the +x direction points to the NE, while in b), the +x direction points in the NW direction.

Chapter 3

Perdigão Flow Characteristics

Placing CLAMPS inside the valley allowed for the collection of a continuous dataset documenting conditions within and above the valley. Using this dataset, it is possible to identify different patterns in the data and characterize the dominant flow regimes.

3.1 Local Wind Characteristics

The predominant wind directions near Perdigão are heavily influenced by the surrounding terrain. Perdigão is located between two mountain ranges: the Serra de Estrela to the NNW and the Serra de São Mamede to the SE. The area in between these two ranges has a gentle slope to the SW that can have an influence on flow patterns.

Figures 3.1 and 3.2 show the wind roses from the VAD scans performed by the CLAMPS DL at key heights during the campaign. There are some interesting differences that occur during the day (Figure 3.1) and night (Figure 3.2). At the lowest VAD level (70 m AGL), winds are generally directed in the along valley direction (i.e., NW and SE). Overnight, the southeasterly component becomes much more pronounced (Figure 3.2). This is likely due to the slope of the valley to the NW and related drainage flow development, which can be seen in Figure 1.1.

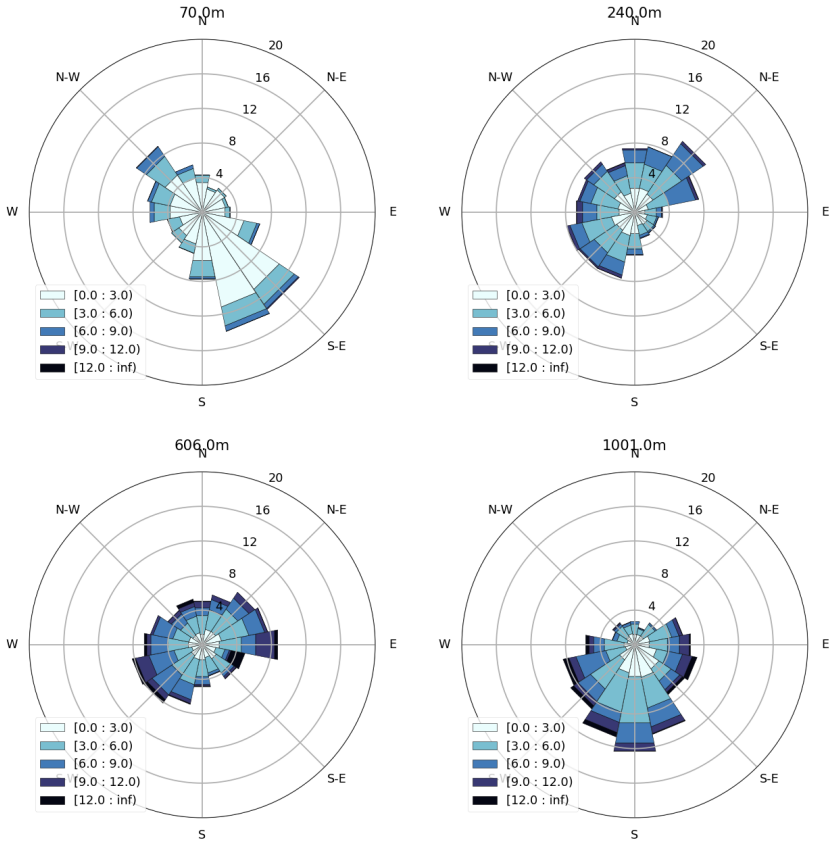

Figure 3.1: Wind roses computed using the CLAMPS DL data collected from 06 UTC to 20 UTC. These times encompass the daytime hours during the campaign. The four heights show flow characteristics well within the valley (70 m), near ridge top (240 m), and in the middle of the boundary layer.

Between 70 m (well within the valley) and 240 m AGL (near ridge top), wind directions change drastically. Similar to the climatology performed with a tower on the SW ridge, winds are generally perpendicular to the ridge axes. At night, north-easterly winds were more commonly observed (Figure 3.2). The preference for north-easterly winds at night is likely due to a katabatic flow down the slope between Serra de Estrela and Serra de São Mamede.

Looking higher still, the effects of the topography in the region are possibly still influencing flow at nearly 600 m AGL since the increase in north-easterly winds

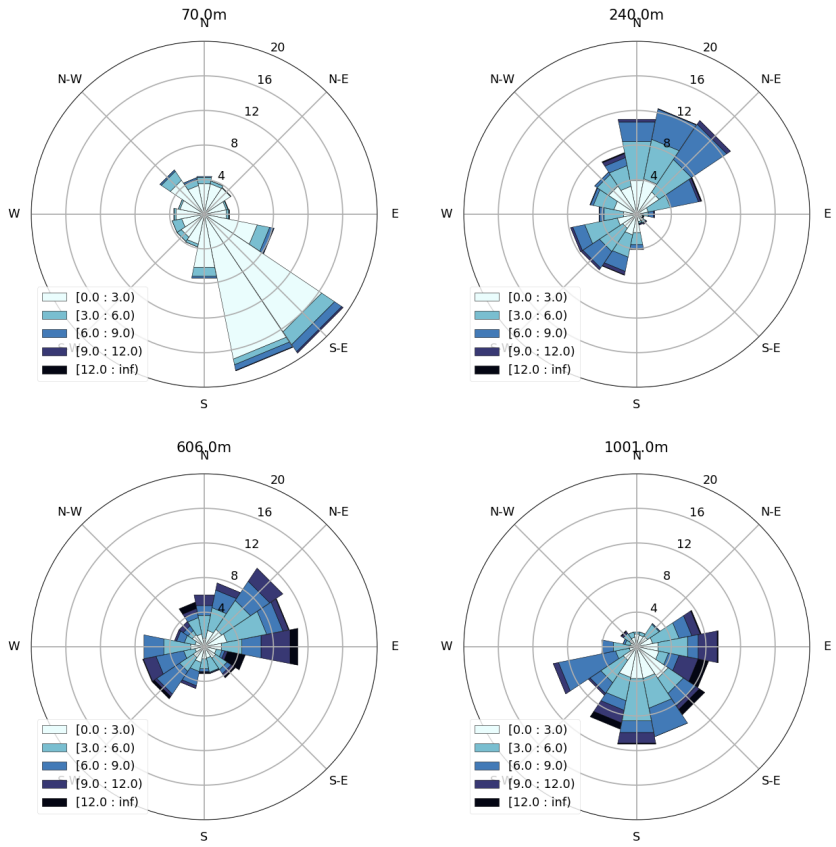

Figure 3.2: Same as Fig. 3.1 but for data collected during the nighttime hours (20 UTC to 06 UTC).

is still apparent overnight (Figure 3.2). Around 1 km, the night and day wind roses become more similar, so this will be considered the level where one finds the background winds. These winds were generally southerly. It should be noted that data from the VADs can be sparse at times at this level, so there are not as many samples in the wind roses at upper levels.

3.2 Thermodynamic Characteristics

While wind roses are useful for analyzing flow in a climatological sense, they do not indicate much about the temporal evolution of wind speeds and directions.

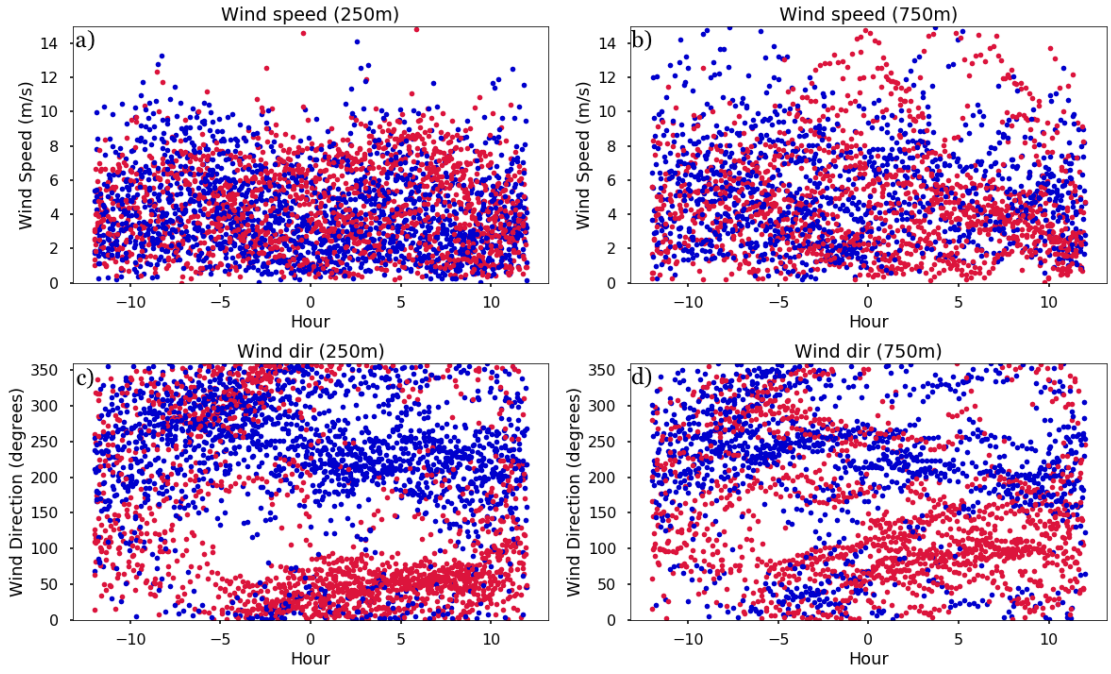

Figure 3.3: Time series of all CLAMPS DL VAD wind speed and wind direction data at two levels, one level near ridge height and one level close to the background wind level discussed in Section 3.1. The x-axis is relative to 00 UTC (e.g. -2 would be 22 UTC). Colors are based on the average wind direction near ridge height from 0 to 6 UTC during a given night with red being north-easterly and blue being south-westerly.

Also, there is no way to relate wind roses to the thermodynamic data from the AERI and MWR.

Looking at the wind roses in Figures 3.1 and 3.2, it is apparent that there is a diurnal pattern in wind speed and direction. Figure 3.3 shows the same data as the wind roses only as 24 hour time series plotted between 12 UTC to 12 UTC (Note: Local time in Perdigão during the experiment is UTC+1, so midnight local time is 01 UTC). The coloring is based on the average wind direction at ridge height from 0 to 6 UTC: red is from days with an average wind direction from the NE (where NE is defined as greater than 318 degrees but less than 138 degrees to

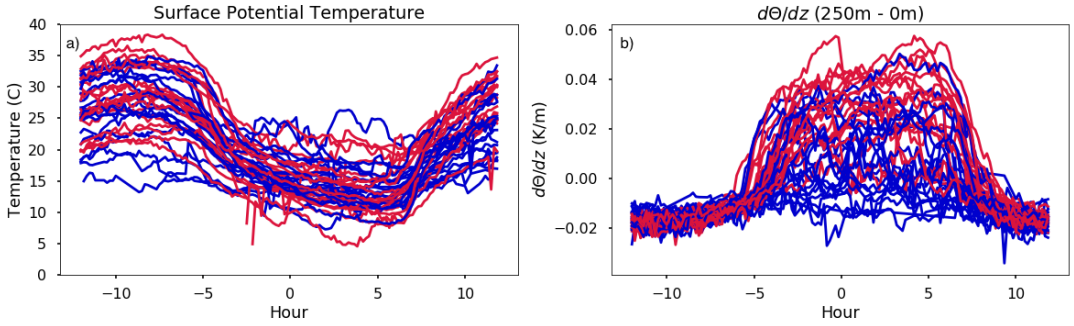

Figure 3.4: Timeseries of a) surface potential temperature and b) $\frac{d\theta}{dz}$ calculated from the surface to approximately ridge height using version 1 of the AERI data. The x-axis is relative to 00 UTC (e.g. -2 would be 22 UTC). Colors are based on the average wind direction near ridge height from 0 to 6 UTC during a given night with red being north-easterly and blue being south-westerly.

line up with the ridge axis), and blue is from days with an average wind direction from the SW (where SW is defined as greater than 138 degrees but less than 318 degrees). The nocturnal, bimodal behavior of the winds is clearly visible in Figure 3.3c. The slope of the valley between Serra de Estrela and Serra de São Mamede is likely the cause of this bimodal behavior. It is still somewhat present in the mid- to upper-levels (Figure 3.3d), though the wind direction starts to converge to the background southerly winds at this level. No clear patterns immediately become apparent from the wind speeds in Figure 3.3a and b.

Figure 3.4 shows data from the AERI using the same wind direction thresholds to determine color. By applying the wind direction threshold, it shows that nights with a more north-easterly wind are generally characterized by larger stability within the valley (Figure 3.4b). There is not any obvious pattern observed in the surface potential temperatures however.

Since stability and wind direction seem to be correlated, it makes sense to analyze based on stability as well. Figure 3.5 shows the same data as Figure 3.4, but categorized based on $\frac{d\theta}{dz}$ inside the valley. Applying the same threshold to the

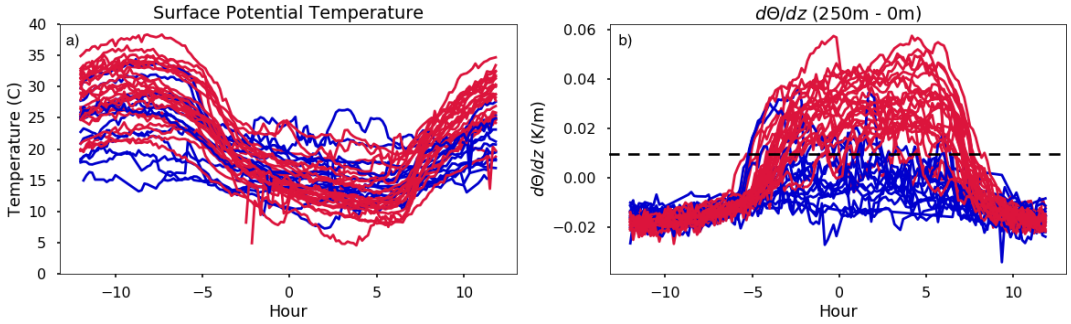

Figure 3.5: Same as Figure 3.4, but the red color now represents nights where the average $\frac{d\theta}{dz}$ was greater than .01 K/m from 0 to 6 UTC.

wind speed and direction data (Figure 3.6) brings out some interesting features in the time series of wind speed and direction near ridge top.

The most apparent feature that appears is the change in wind direction that occurs near ridge height during the evening transition (Figure 3.6c). From around -6 UTC to 0 UTC, winds veer with time. There also appears to be a drop in wind speed during this same time (Figure 3.6a).

All this lends to the hypothesis that there is some sort of thermodynamic circulation in the region, likely due to the surrounding mountains. More analysis is required on the regional scale to determine exactly what is going on. However, the scope of the present study focuses more on the scale of the ridges, so this will not be pursued further.

3.3 Case Study Selection

While much insight can be gained by considering the dataset as a whole, there was a large number of flow phenomena in and around the ridges that are best analyzed in case studies.

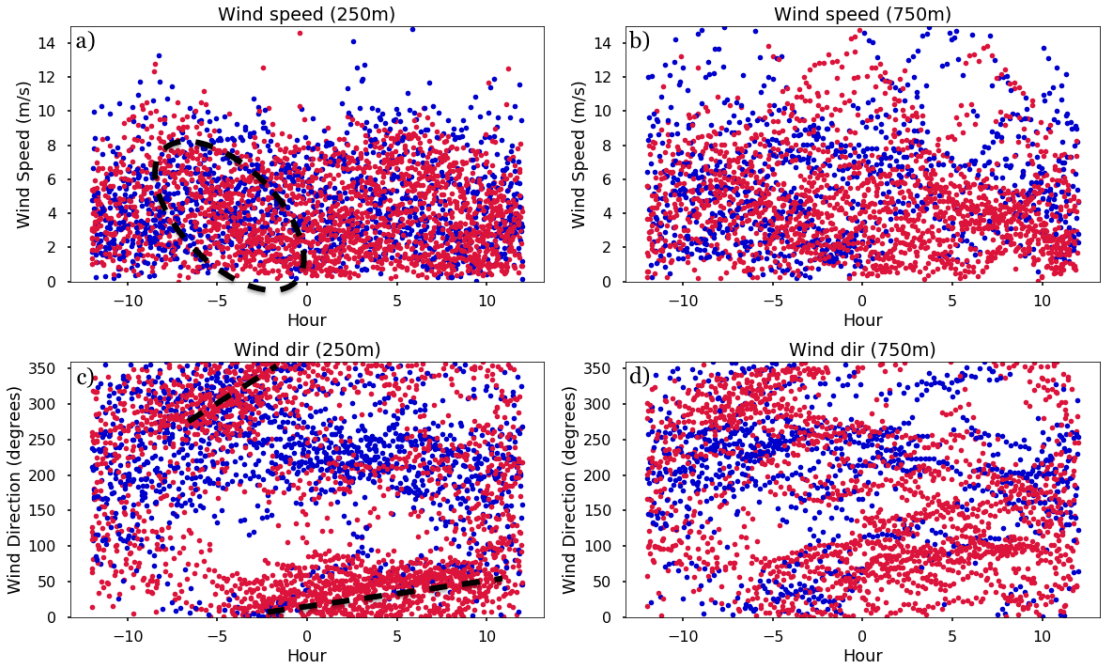

Figure 3.6: Same as Figure 3.3, but the red color now represents nights where the average $\frac{d\theta}{dz}$ was greater than .01 K/m from 0 to 6 UTC.

Immediately following the experiment, data from CLAMPS were visually inspected to identify interesting phenomena inside the valley. The phenomena observed by CLAMPS included gravity waves, recirculations, wakes, low-level jets, turbulence within the valley, and slope flows. Table 3.1 shows how many days of the campaign these phenomena were observed by the CLAMPS system.

By nature of the complexity of the terrain, slope flows were observed during most nights. Additionally, low-level jets were quite common near ridge height, which caused gravity waves and recirculations in the valley.

Data from May 22, 2017 in Figure 3.7 contains many of the phenomena: there is a low level jet, recirculation, downslope flow, and a wave that forms. By cataloging days with features like these and recording background conditions and data quality, it is possible to extract a few case studies to concentrate on.

Table 3.1: Table outlining the number of days where particular phenomena were observed using the CLAMPS system.

	Gravity wave	Recirc-ulation	Turbine Wake	Jet	Turbulent in valley	Slope Flow
Yes	21	23	3	24	12	31
No	13	12	26	12	24	6
Maybe	6	5	11	4	4	3

3.3.1 May 22-23, 2017

During this time period, Perdigão was under a strong 500 mb ridge following the passage of a quick shortwave trough the day before. Upper level winds were weak and variable in direction. This time period presents a good all around case to study since many of the commonly observed phenomena occurred over this time period (see Figure 3.7).

CLAMPS observations over this time period are shown in Figure 3.8, which shows time-height plots of potential temperature, wind speed and direction, and average vertical velocities collected in the center of the valley by CLAMPS. A stable layer forms within the valley. This case has relatively strong winds above ridge height due to the presence of a low-level jet (Figure 3.8b). Around 01 UTC and through the rest of the night, negative vertical velocities are observed throughout the column (Figure 3.8d). Also at this time, some turbulence is present inside the valley as the low level jet picks up speed at ridge height. In general, winds at ridge height are approximately from the NE through the night. Slightly above ridge height winds veered with time (Figure 3.8c).

3.3.2 May 7-8, 2017

During this time, there was a low pressure system off the coast of the Iberian Peninsula and a ridge over Perdigão. Aloft, winds over the IOP site were from the southwest at 30 kts around 500 mb. The regional scale flows discussed in Section 3.1 can introduce unique layering of wind speeds and direction near the ground.

The complexity of the flow for May 7-8th is shown in Figure 3.9. Generally, winds were from the northeast during the night of the 7th (Figure 3.9c). On the 8th, winds veered through the night and became very weak at ridge height (Figure 3.9b). Wind directions in the valley were quite variable since the mean wind interacted with various slope flows occurring inside the valley.

Numerous periods of strong vertical motion were observed over the CLAMPS site due to waves and circulations forming as a result of the terrain. On the 8th, a unique wave feature was observed along with a re-circulation within the valley. This occurred during the period of relatively low wind speeds around 05 UTC. A similar feature did not appear often during the rest of the IOP and lends itself well as a good test case for virtual tower retrievals since they are better able to capture the complex evolution over time and space (Chapter 4).

The 8th was also characterized by a very strong and shallow stable layer at the surface, which caused down-valley thermal flows.

3.3.3 May 20-21, 2017

During this period, Portugal was downstream of a 500 mb trough. Flow at 850 mb was from the south at 20 kts.

This night is different from the previous two cases. Wind speeds above ridge height were considerably stronger than usual, among the highest wind speeds observed from CLAMPS during the IOP. The maximum wind speed was nearly 20 ms^{-1} (Figure 3.10b) and was located around 500 m above the top of the ridge.

Wind directions were from the NE at ridge height and from the east slightly above ridge height, this stayed relatively constant through the night (Figure 3.10c).

Additionally, there was no strong low level temperature inversion (Figure 3.10a) inside the valley. However, it was still stable through the depth of the valley. The high wind speeds created very strong downward motion throughout the depth of the high wind speeds (Figure 3.10d) and created relatively strong turbulence within the valley (Figure 3.10e) which likely inhibited the evolution of a strong low level inversion and the associated down valley flow. No waves were observed this night likely due to the high wind speeds causing flow to simply skip over the valley.

3.3.4 May 21-22, 2017

The last case considered was affected by a weak 800 mb low pressure system that was associated with the incoming trough mentioned in Section 3.3.3. The passing of this low can be seen in Figure 3.11c at around the 1 km level and above. There was shift in wind direction that continued through the night that started slightly before 00 UTC. Wind speeds were generally not greater than 10 ms^{-1} and grew weaker as the night went on (Figure 3.11b).

One interesting feature is the pocket of turbulence above the ridge top from 3 UTC to 6 UTC (Figure 3.11e). This feature is associated with a sharp wind shift in height and upward motion (Figure 3.11). One interesting feature in the cross valley RHI also presents itself during this time period. Flow going over the SW ridge appeared to be relatively laminar, but as it traveled over the second ridge, it became more turbulent (Figure 3.12).

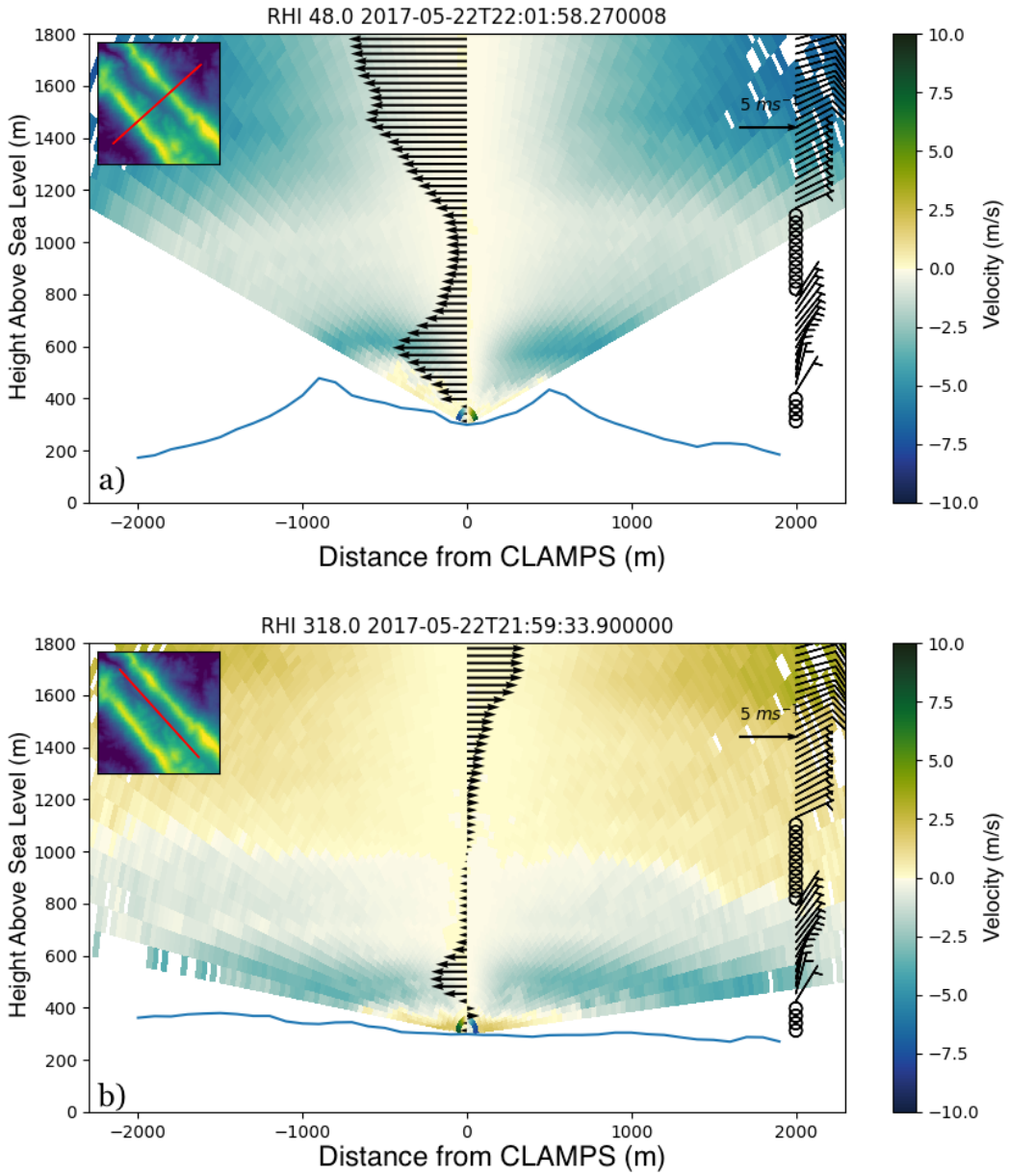

Figure 3.7: Same as Figure 2.4, except for 22 UTC on May 22, 2017.

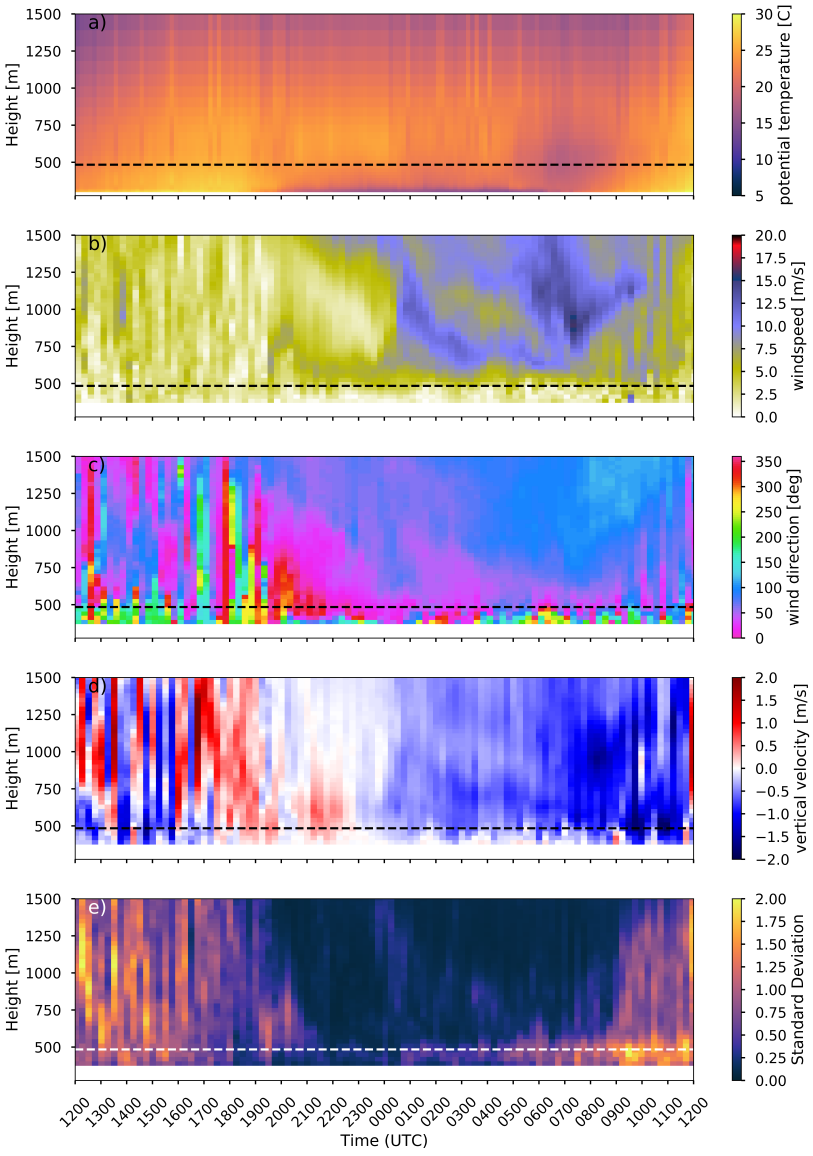

Figure 3.8: Same as Figure 2.3, except for the time period from 12Z May 22nd to 12Z on May 23rd.

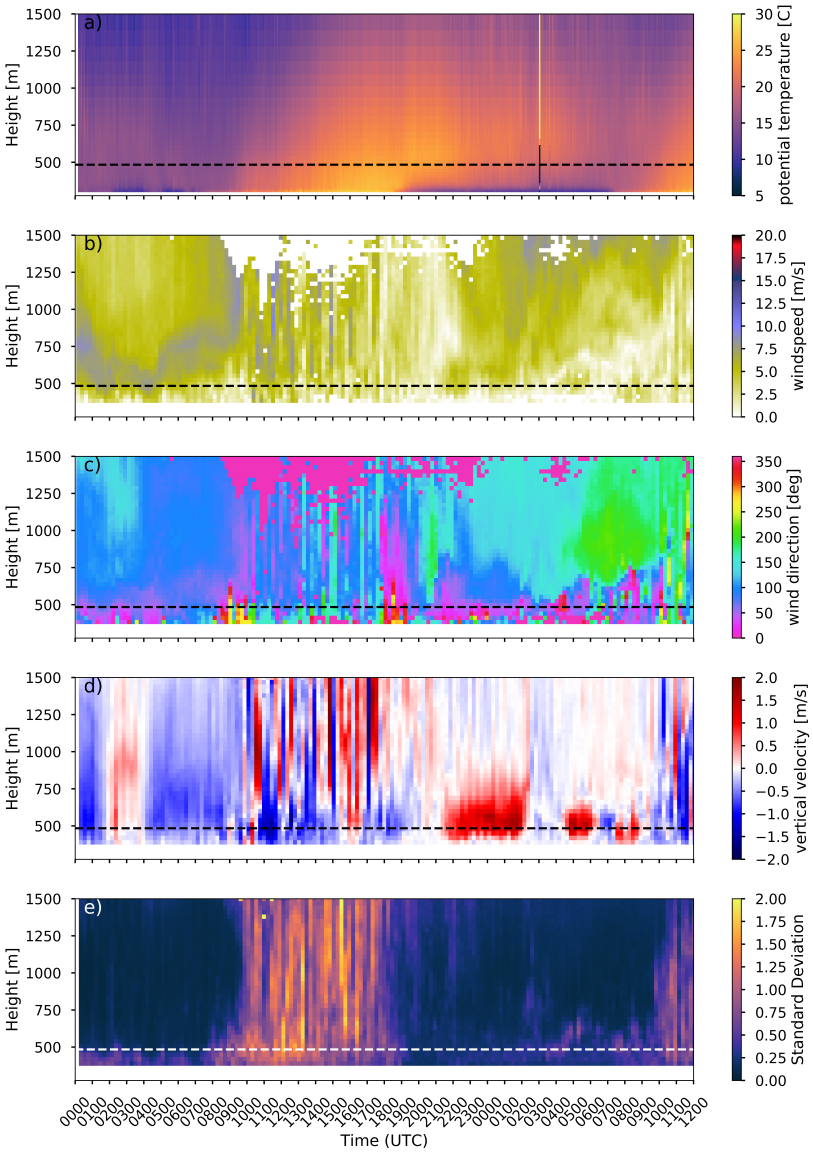

Figure 3.9: Same as Figure 2.3, except for May 7th at 00 UTC to May 8th at 12 UTC. The AERI retrival in a) is a special 5-minute time resolution from the V2 dataset. Note the strong, shallow inversion in the valley and the weak wind overnight on the 8th, while the winds on the night of the 7th are much stronger and the potential temperature profile is more well mixed.

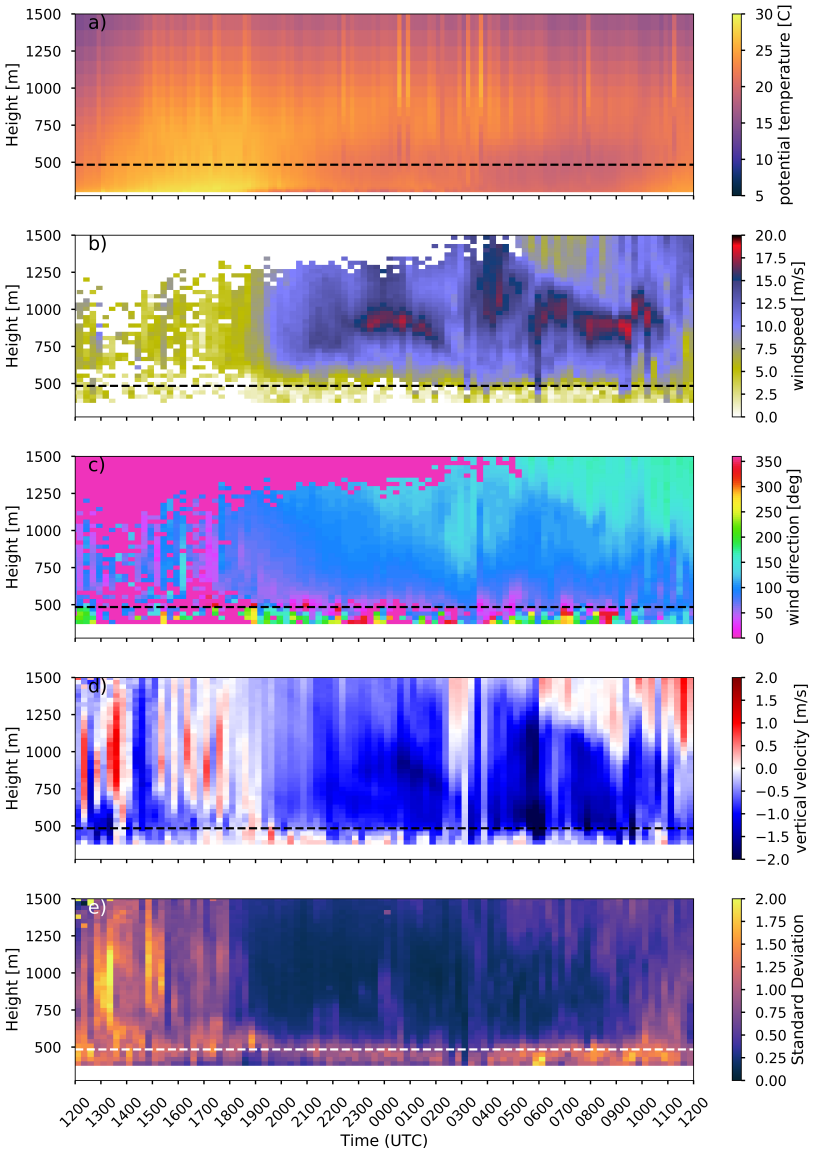

Figure 3.10: Same as Figure 2.3, except for May 20st at 12 UTC to May 21nd at 12 UTC.

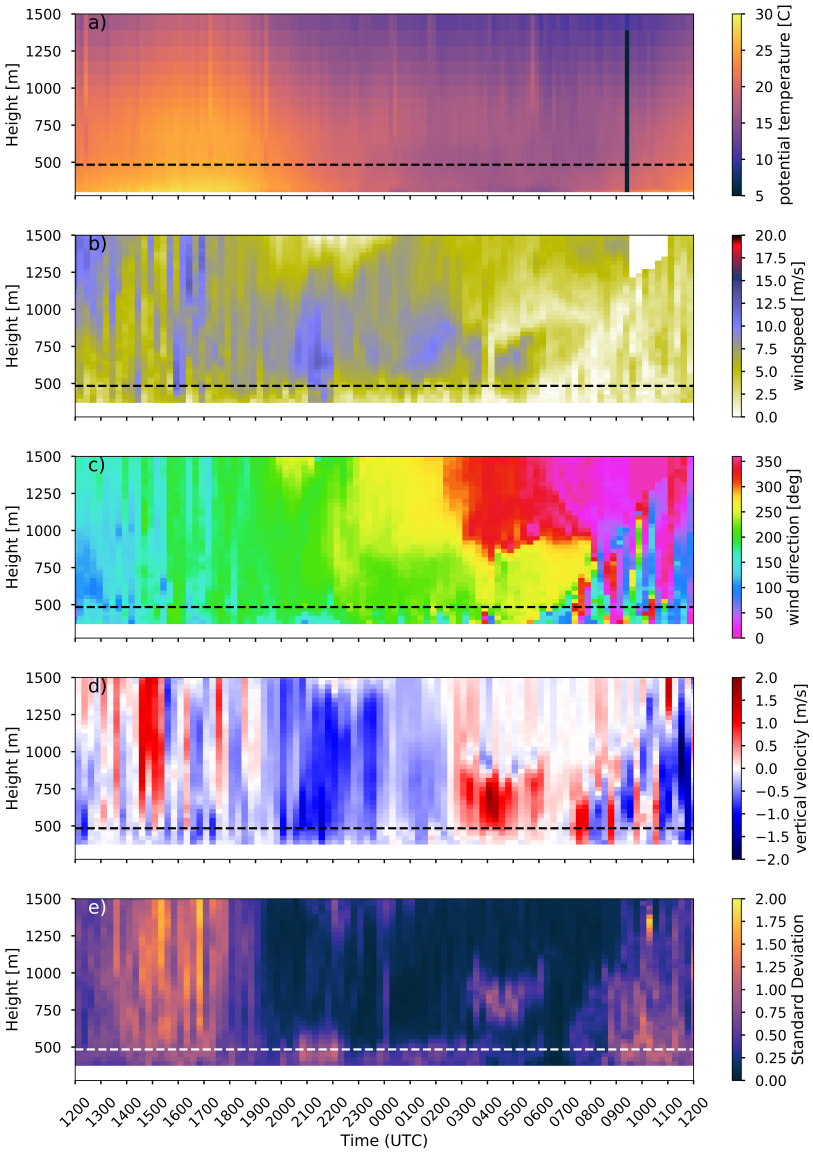

Figure 3.11: Same as Figure 2.3, except for May 21st at 12 UTC to May 22nd at 12 UTC.

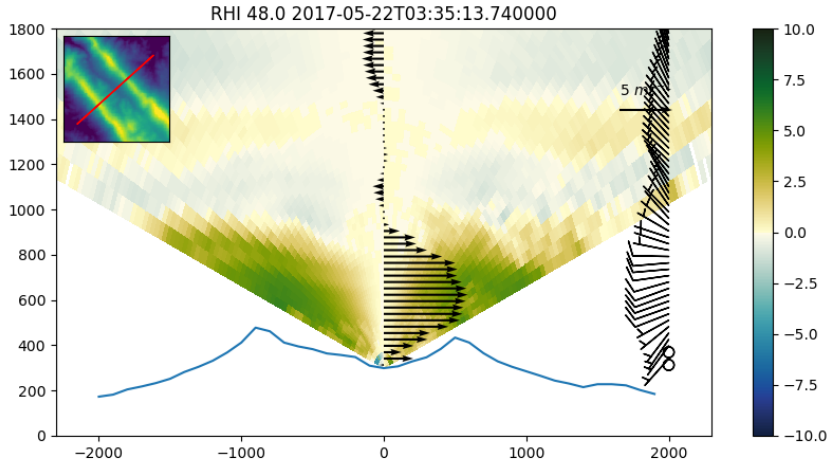

Figure 3.12: Same as figure 3.7a, except for May 22, 2017 during the period of turbulence above ridge height. Notice how flow over the ridge at -900 m appeared smooth while flow at approximately 600 m appeared turbulent as it went over the ridge.

Chapter 4

Virtual Tower Analysis

4.1 Doppler Lidars

Multiple DL configurations were combined to retrieve the 3D wind vector at various locations in the valley. In total, 6 DLs from 3 different institutions were combined to retrieve virtual towers four times per hour. See Table 4.1 for more information about the scan strategies used for each DL.

4.1.1 OU DL

As mentioned in Section 2.1.1, OU deployed CLAMPS at the lower Orange site (Figure 4.1) located inside the valley during the IOP. CLAMPS's DL performed both cross- (N to SW) and along-valley (NW to SE) RHI scans every 15 minutes. In addition, a 70 degree PPI scan was performed every 15 minutes proceeding the RHIs. The remainder of the time, the DL was in vertical stare mode to obtain vertical velocity statistics.

Table 4.1: Characteristics of the RHI scans performed by each DL in Perdigão.

Lidar ID	Azimuth	Min. Elevation	Max Elevation	Update Time
OU CLAMPS	318 °	7.5 °	175 °	15 min
DLR 85	236.1 °	-7.4 °	45.1 °	∼30 s
DLR 86	236.4 °	8.5 °	122 °	∼30 s
WS2	54.7 °	-18.8 °	15.7 °	∼30 s
WS5	52.3 °	-12.8 °	21.7 °	∼30 s
WS6	42.2 °	-16.8 °	17.7 °	∼30 s

4.1.2 The German Aerospace Center (DLR) DLs

The German Aerospace Center (DLR) contributed three Leosphere Windcube 200S scanning DLs upgraded with the Technical University of Denmark's (DTU) WindScanner software. Two of these DLs performed continuous RHI scans in the cross-valley direction, which resulted in an RHI approximately every 30 seconds. One of these DLs was located up on top of the NE ridge (DLR85) and performed RHI scans to the SW, capturing one horizontal component of the wind. The other DL (DLR86) was located on the slope of the NE ridge and performed RHIs to the SW as well (Figure 4.1).

4.1.3 DTU DLs

DTU operated eight DLs of the same kind as DLR on top of the ridges. Six of these were configured to do co-planar scans inside the valley so the horizontal wind in the plane and the vertical velocity could be retrieved. For this study, only the DLs from each co-planar cross section that reached deeper into the valley were used. This resulted in 3 possible two-dimensional horizontal wind retrievals using

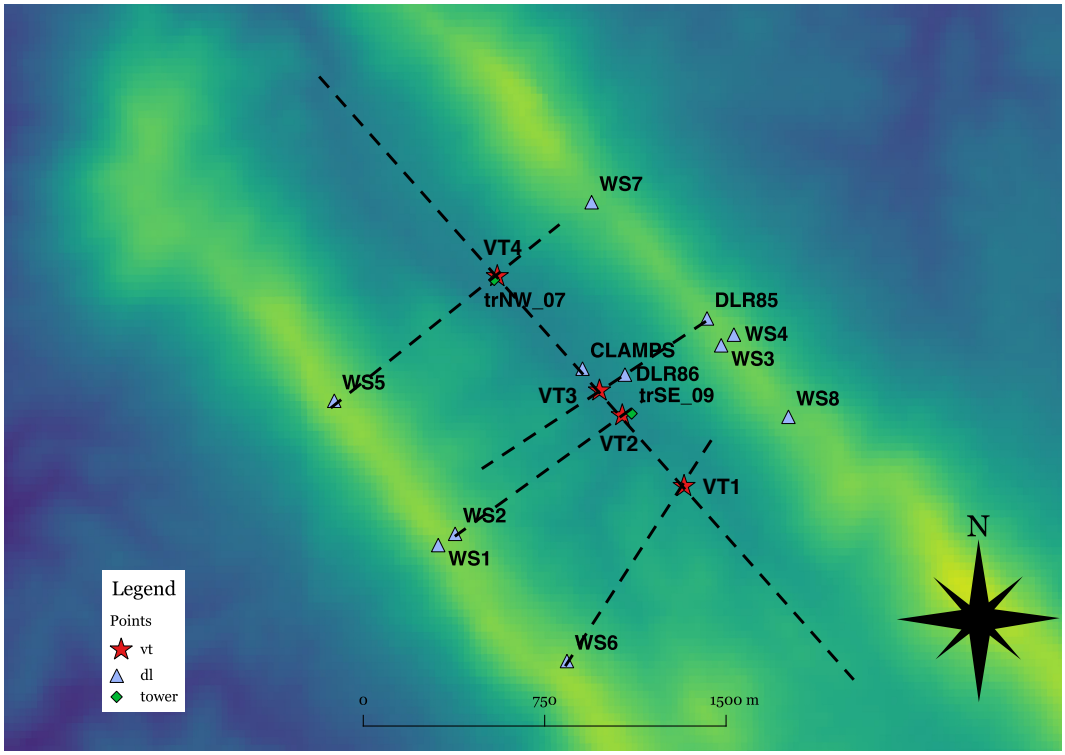

Figure 4.1: Map of DLs, meteorological towers, and virtual towers at the Perdigão site.

WS2, WS5, and WS6 (Figure 4.1). These DLs also operated in a continuous scan mode and produced a new RHI every 30 seconds.

4.1.4 Virtual Towers

The RHIs from DLR85 and DLR86 overlapped in a co-planar fashion, so by combining these DLs with the OU DL scans, it is possible to retrieve the three-dimensional wind field in the form of a virtual tower where the three planes intersect (VT3).

Regarding the DTU DLs, since the scans were coplanar, the line-of-sight (LOS) velocities measured by both DLs essentially were the negative of each other and did not provide any additional component of the wind field. In order to maximize the number of heights measured, only the DLs from each co-planar cross section

that reached deeper into the valley were used. This resulted in 3 possible two-dimensional horizontal wind retrievals using WS2 (VT2), WS5 (VT4), and WS6 (VT1).

In total, four virtual towers distributed along the valley (Figure 4.1) were retrieved every 15 minutes when the CLAMPS DL performed its along-valley RHI. The virtual towers typically cover heights from 50 m to 600 m above the valley floor based on the minimum and maximum height of RHI intersection. None of the DLs used in the retrievals scanned in a coordinated fashion, but it was still possible to accurately measure mean flow characteristics (Choukulkar et al., 2017).

4.2 Methods

Data from each DL were first converted to a common coordinate system. Once the XY location of the crossing RHIs was determined, the gates at that point were linearly interpolated to set heights where the 3-D wind vector could be retrieved. These heights were manually determined based on plots of where the RHIs overlap; the vertical spacing of the retrievals is 10 m. The azimuth and elevation of the virtual tower points is calculated relative to the individual DLs. Retrieving the 3D (2D) wind vector is as simple as solving the 3D (2D) transformation matrix for the line of sight (LOS) velocity vector to get:

$$\begin{bmatrix} u \\ v \\ w \end{bmatrix} = \begin{bmatrix} \sin\theta_1 \cos\phi_1 & \cos\theta_1 \cos\phi_1 & \sin\phi_1 \\ \sin\theta_2 \cos\phi_2 & \cos\theta_2 \cos\phi_2 & \sin\phi_2 \\ \sin\theta_3 \cos\phi_3 & \cos\theta_3 \cos\phi_3 & \sin\phi_3 \end{bmatrix}^{-1} \begin{bmatrix} V_{r1} \\ V_{r2} \\ V_{r3} \end{bmatrix} \tag{4.1}$$

where u is the velocity in the east-west direction, v is the velocity in the north-south direction, w is the vertical velocity, V_{ri} is the radial velocity measured by the ith DL, ϕ_i is the elevation, and θ_i is the azimuth angle used by the DL.

Temporal resolution of the virtual towers was limited to time resolution of the CLAMPS RHI. Since the scans were not coordinated to sample the same volume of space simultaneously, a somewhat loose time window of 60 s was used. That is, all scan times must be within 60 s of each other, otherwise the assumption that the beams are looking at the same flow could be invalidated.

4.2.1 Uncertainty Analysis

An analysis of the possible uncertainties contained in the retrieval was performed using an idealized uncertainty scheme derived from the methods used in Hill et al. (2010):

$$\epsilon_{u_i} = \left[\sum_{j=1}^{N} \left(\frac{\partial u_i}{\partial r_j} \right)^2 (\epsilon_{r_i})^2] \right]^{1/2} ; i = 1, 2, 3 \tag{4.2}$$

where ϵ_{r_i} is the uncertainty due to random error in each DL line-of-sight wind speed measurement, u_i is the Cartesian velocity component of the wind, and r_j is the LOS velocity vector for each DL. This results in a formula for the error given a combination of the various azimuths, elevations, and ranges for each DL (Equations 4.3-4.6).

$$C = [\sin(\phi_1) * (\cos(\phi_2) * \cos(\phi_3) * \sin(\theta_2) * \cos(\theta_3) - \cos(\phi_2) * \cos(\phi_3) * \cos(\theta_2) * \sin(\theta_3)) + \cos(\phi_1) * \cos(\theta_1) * (\sin(\phi_2) * \cos(\phi_3) * \sin(\theta_3) - \cos(\phi_2) * \sin(\phi_3) * \sin(\theta_2)) + \cos(\phi_1) * \sin(\theta_1) * (\cos(\phi_2) * \sin(\phi_3) * \cos(\theta_2) - \sin(\phi_2) * \cos(\phi_3) * \cos(\theta_3))]^2 \tag{4.3}$$

$$\epsilon_u = [(\epsilon_r^2 * (\cos(\phi_2) * \sin(\phi_3) * \cos(\theta_2) - \sin(\phi_2) * \cos(\phi_3) * \cos(\theta_3))^2)/C + (\epsilon_r^2 * (\sin(\phi_1) * \cos(\phi_3) * \cos(\theta_3) - \cos(\phi_1) * \sin(\phi_3) * \cos(\theta_1))^2)/C + (\epsilon_r^2 * (\cos(\phi_1) * \sin(\phi_2) * \cos(\theta_1) - \sin(\phi_1) * \cos(\phi_2) * \cos(\theta_2))^2)/C]^{1/2} \tag{4.4}$$

$$\epsilon_v = [(\epsilon_r^2 * (\sin(\phi_2) * \cos(\phi_3) * \sin(\theta_3) - \cos(\phi_2) * \sin(\phi_3) * \sin(\theta_2))^2)/C + (\epsilon_r^2 * (\cos(\phi_1) * \sin(\phi_3) * \sin(\theta_1) - \sin(\phi_1) * \cos(\phi_3) * \sin(\theta_3))^2)/C + (\epsilon_r^2 * (\sin(\phi_1) * \cos(\phi_2) * \sin(\theta_2) - \cos(\phi_1) * \sin(\phi_2) * \sin(\theta_1))^2)/C]^{1/2} \tag{4.5}$$

$$\epsilon_w = [(\epsilon_r^2 * (\cos(\phi_2) * \cos(\phi_3) * \sin(\theta_2) * \cos(\theta_3) - \cos(\phi_2) * \cos(\phi_3) * \cos(\theta_2) * \sin(\theta_3))^2)/C + (\epsilon_r^2 * (\cos(\phi_1) * \cos(\phi_3) * \cos(\theta_1) * \sin(\theta_3) - \cos(\phi_1) * \cos(\phi_3) * \sin(\theta_1) * \cos(\theta_3))^2)/C + (\epsilon_r^2 * (\cos(\phi_1) * \cos(\phi_2) * \sin(\theta_1) * \cos(\theta_2) - \cos(\phi_1) * \cos(\phi_2) * \cos(\theta_1) * \sin(\theta_2))^2)/C]^{1/2} \tag{4.6}$$

4.3 Results

4.3.1 Sensitivity of Uncertainty to Elevation

For this study, it was assumed that ϵ_{r_i} was .2 ms^{-1}. This is based on prior experience with the systems used. Results from the uncertainty scheme when all DLs are operating correctly are shown in Table 4.2.

Note that with increasing height (i.e. as beams scan at a more vertical elevation), uncertainties in the horizontal wind components get larger and uncertainties in the vertical velocity get smaller. Also note that the errors in horizontal wind components are much larger in the 3D retrieval than in the 2D retrievals. This is largely due to the proximity of the virtual tower to the OU DL; gates at much higher elevation angles must be used, meaning less of the horizontal component of the wind is contained in the LOS velocity, therefore there is more uncertainty in the true value.

Looking at things more closely, it is possible to tease out how the error changes with elevation angle. Thus, conclusions can be drawn about how far away an optimal DL placement would be given certain configurations. It is also possible to see how different the uncertainties in the retrievals can be in 2D vs 3D retrievals.

To demonstrate the utility of this, an idealized setup that closely mimics the setup in Perdigão is used. A schematic of the setup can be found in Figure 4.3. For the experiment, the uncertainty at a point on a virtual tower at height R is calculated. DL1 and DL2 are fixed in place, but DL3 is allowed to move in range away from the tower, thereby decreasing the elevation angle required to observe the same point. This setup is meant to mimic the DL placements for the 3D tower. For 2D uncertainty calculations, only DL1 and DL3 are used.

Figure 4.4 shows the results for R=300 m and H=200 m with x1=1.75R and x2=.4R, which was determined from actual positions of DLR85, DLR86, and the

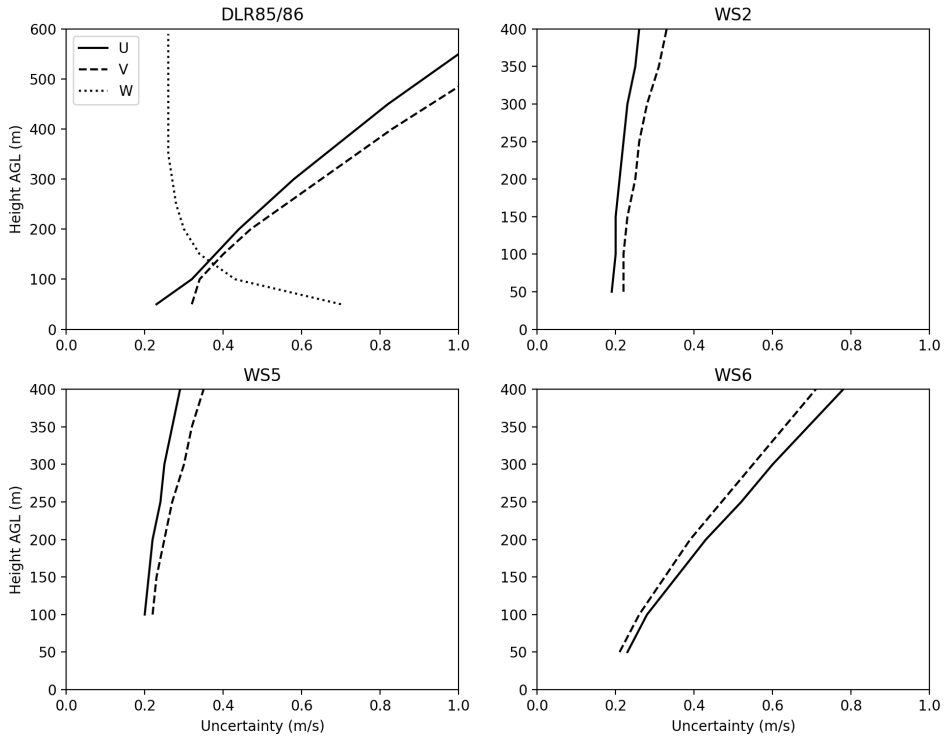

Figure 4.2: Uncertainties of the virtual towers associated with the locations of the DLs.

resulting virtual tower. A height of R=300 m was chosen because this is approximately the same height of the highest measurement point on a meteorological tower in the IOP. Since one goal of the virtual towers is to extend the maximum measured height, it is important to characterize the uncertainty at those levels.

Comparing the values from Figure 4.4 to those in Table 4.2 revals close agreement, which lends credit to the idealized setup.

There are obvious differences in the retrievals of 2D and 3D uncertainty. 2D retrievals tend to have less uncertainty using this scheme. Since most of the vertical component comes from DL2, ϵ_w does not change much as DL3 is moved further away from the virtual tower (Figure 4.4c).

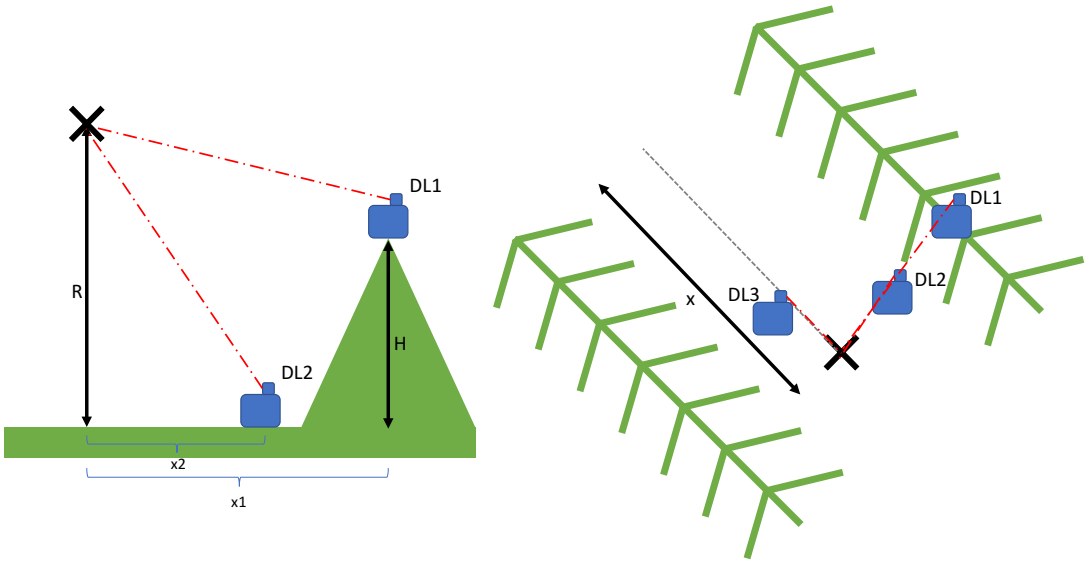

Figure 4.3: Depiction of the setup used to test the sensitivity of the uncertainty in the 3D tower to the elevation angle of the CLAMPS DL.

In Perdigão, the 3D tower (DLR85/86) is located in the range where uncertainty starts to rapidly increase with increased elevation angle (Figure 4.4a and b). With this configuration, the v-component tends to have more uncertainty associated with it because all the DLs are pointing more in the -v direction. If one of the DLs were to point in such a way that it had a component in the +v direction, some of the uncertainty would be mitigated.

By shifting the frame of reference in such a way that DL3 is stationary and DL1 moves along the ridge, it is easy to see WS2 and WS6 are in positions that are well suited for 2D retrievals.

Idealized setups like this could be used in future field campaigns to try and mitigate uncertainty in virtual tower setups.

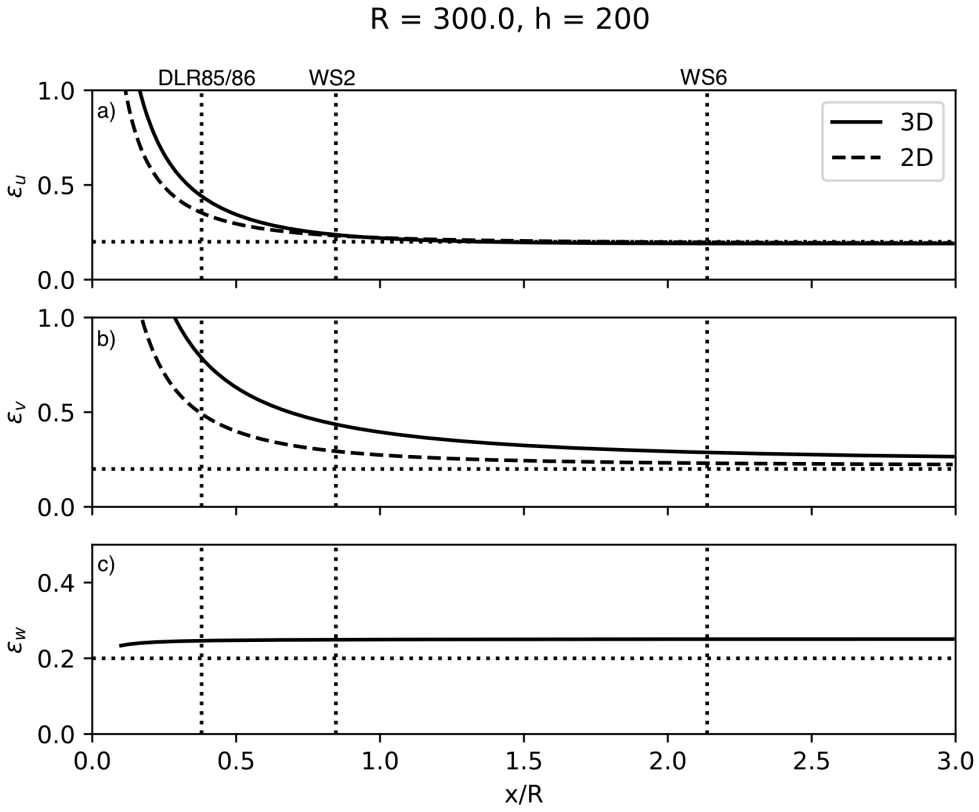

Figure 4.4: Results of the the uncertainty analysis for R=300 and H=200 with $\epsilon_r = .2ms^{-1}$. Vertical dotted lines are locations of virtual towers. The x axis is normalized by the height of the point being observed.

4.3.2 Comparison of Wind Retrieval Techniques

As mentioned before, the traditional DL technique for retrieving the wind speed and direction is the VAD or the DBS technique. However, in the overnight hours of the Perdigão campaign, the assumption of horizontal homogeneity is violated due to gravity waves and a recirculation created by the terrain. This is especially prominent at the lowest levels of the VAD. Due to the multitude of instruments in the valley, comparisons can be made between various methods of wind estimation from DLs and to sonic anemometers spread throughout the valley.

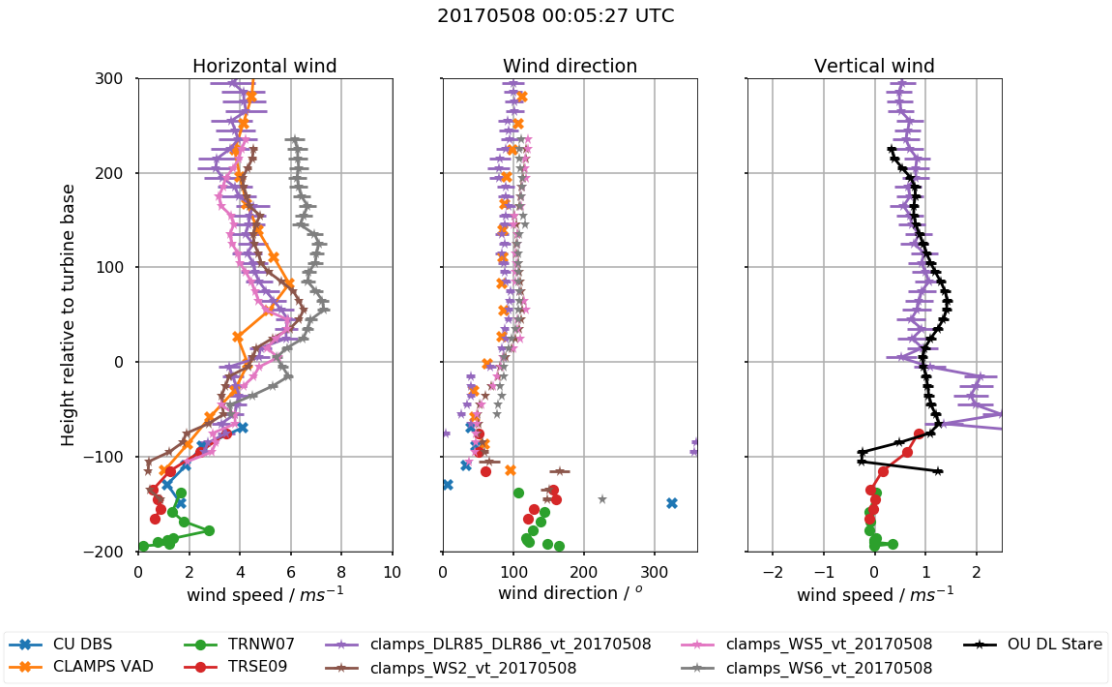

Figure 4.5: Profiles from each of the different wind estimation techniques. Note the height axis is relative to the base of the wind turbine. In general, the methods agree well above the ridge, but results are inconsistent 100 m below ridge height. Tower data is still preliminary.

Figure 4.5 shows how the traditional techniques can produce erroneous retrievals in complex terrain. In addition to the DLs used in the virtual tower retrievals, the University of Colorado (CU) operated a Leosphere V1 Windcube Profiling DL at the Lower Orange Site, very close to the OU DL. The CU DL measured the wind speed and direction using the DBS technique.

Generally, all the different methods agree well above ridge height. Once the profiles get approximately 100 m below ridge height, the different techniques start to disagree. Wind speeds stay relatively consistent between each technique below ridge height, but the directions are highly variable. In particular, the wind directions from the CU DBS scan differ greatly from the towers, both virtual and

physical. The virtual towers correctly detect down-valley flow that was often observed in RHI scans during the IOP. The OU VAD does a decent job, but does not have any data points close to the ground. In other cases, the OU VAD can also differ greatly from the virtual towers. This lends credit to the idea that these scan types are not fulfilling the required assumptions to correctly measure wind speed and direction.

The vertical velocities from the 3D tower and the OU DL stare also agree quite well above ridge height. The vertical velocity profiles diverge at the same level as the wind speed and direction, around -100 m. The differences could be due to each measurement representing a different time. The tower data are 5 minute averages, while the OU DL stare data and the CLAMPS/DLR virtual tower are instantaneous measurements at slightly different locations, so naturally some differences are to be expected.

It is quite promising to see the 2D retrievals match well with the towers despite there being large fluctuations of vertical motion in the center of the valley that could contribute to the LOS velocities and affect the horizontal measurements.

4.3.3 Spatial Analysis

To help summarize the results of this study, data from interesting cases early in the Perdigão IOP are presented. To highlight how useful the virtual towers can be for measuring the spatial variability of features along the valley, a moderately complex case, May 7-8th 2017, was chosen. More details of this night were discussed in Section 3.3.2. The more common case from May 22nd and 23rd (Section 3.3.1) is also analyzed.

One of the main reasons Vale do Cobrão was chosen for the experiment was the quasi-two-dimensional nature of the ridges. This natural orientation was thought to be the best way to represents a series of periodic rolling hills and that flow

perpendicular to the ridges could also be considered quasi-2D. In order to test how effective this idea is in reality, it is best to think of wind components in the cross-valley and along-valley sense.

4.3.3.1 Case 1

The first case analyzed was from the May 7-8th time period discussed in Section 3.3.2. The night of May 7th had higher wind speeds at ridge height than the night of May 8th, so times from both nights was analyzed.

Analysis of the virtual towers coupled with the cross-valley RHIs from the DLR and CTU DLs often shows that the flow can not be considered entirely 2D. In Figure 4.6, there is a clear terrain-following low level jet that forms. Though it is difficult to tell if it is a jet in the radial velocities, it is apparent in the wind vectors that there is a clear wind speed maxima present around 500 m ASL. Additionally, on the southwestern slope of the valley, a recirculation develops in some of the cross-sections of the valley, but not others. Where the recirculation is present, it reduces wind speeds at the locations of the virtual towers. For example, WS6 and WS2 have cross valley wind speeds 1-2 ms^{-1} lower than the DLR85, especially at the lower tower levels where the recirculation is taking place. This also appears in some of the levels well above the valley.

Looking at the along-valley component of the winds, no clear features stand out. Winds are near zero within the valley. However, though not obviously present in Figure 4.6, a downslope flow is often observed overnight in the along valley RHI from CLAMPS, adding to the three-dimensionality of the flows present in the valley.

Analysis of a different time period further shows the complexity of the flows in the terrain. On the night of May 8, 2017, winds veered rather quickly aloft and weakened closer to the surface (Figure 3.9). Figure 4.7 shows what the cross-

and along-valley flow looked like before the wind speeds dropped. No real wave or recirculations can be seen in the cross-valley direction and cross valley wind speeds are relatively uniform with height. There is a speed max approximately 200 m above ridge height in the along valley direction. An interesting transition occurs and a unique wave forms within the valley once the winds decrease around 05 UTC (Figure 4.8). Like the previous night, there is little along-valley component of the wind below the ridge. This night does show a speed maximum in the down-valley flow in the lowest 20-30 m of the OU RHI scan, which is indicative of the aforementioned downslope flow. Similar to the May 7th case, a recirculation is present inside the valley and has a highly complex structure that differs based on the cross section of the valley. The recirculation looks to be largest in the WS2 cross section, similar to the previous case. This again appears to slow wind speeds upstream of the recirculation.

4.3.3.2 Case 2

The CLAMPS observations from this case were discussed in Section 3.3.1. For this case, WS5 and DLR85 were not operating correctly and had to be excluded from the analysis. Since DLR85 was one of the DLs in the 3D tower, there are only 2D retrievals for this time period. Additionally, a high elevation angle is needed for DLR86 and the CLAMPS DL to create the tower so there is a large amount of uncertainty to the retrievals.

This night was characterized by much stronger winds just above the ridge, especially after 01 UTC (i.e., as reflected in the cross-valley winds depicted in the bottom row of Figure 4.9). Due to this, the recirculation in the valley spanned most of the width of the valley (Figure 4.9). It also did not change much along the length of the valley, which means this time period may be more suited to be considered homogeneous along the length of the valley. The strong shear layer

above the valley likely shielded the valley from impinging flows; instead the jet just skipped over the valley. Therefore the terrain features inside the valley that can cause heterogeneities in the flow had less of an impact. The lack of a strong stable layer inside the valley (see Figure 3.8) also meant there was practically no down-valley flow observed.

Again, in the long valley view, no clear features are identifiable due to the very small component of the wind in this direction.

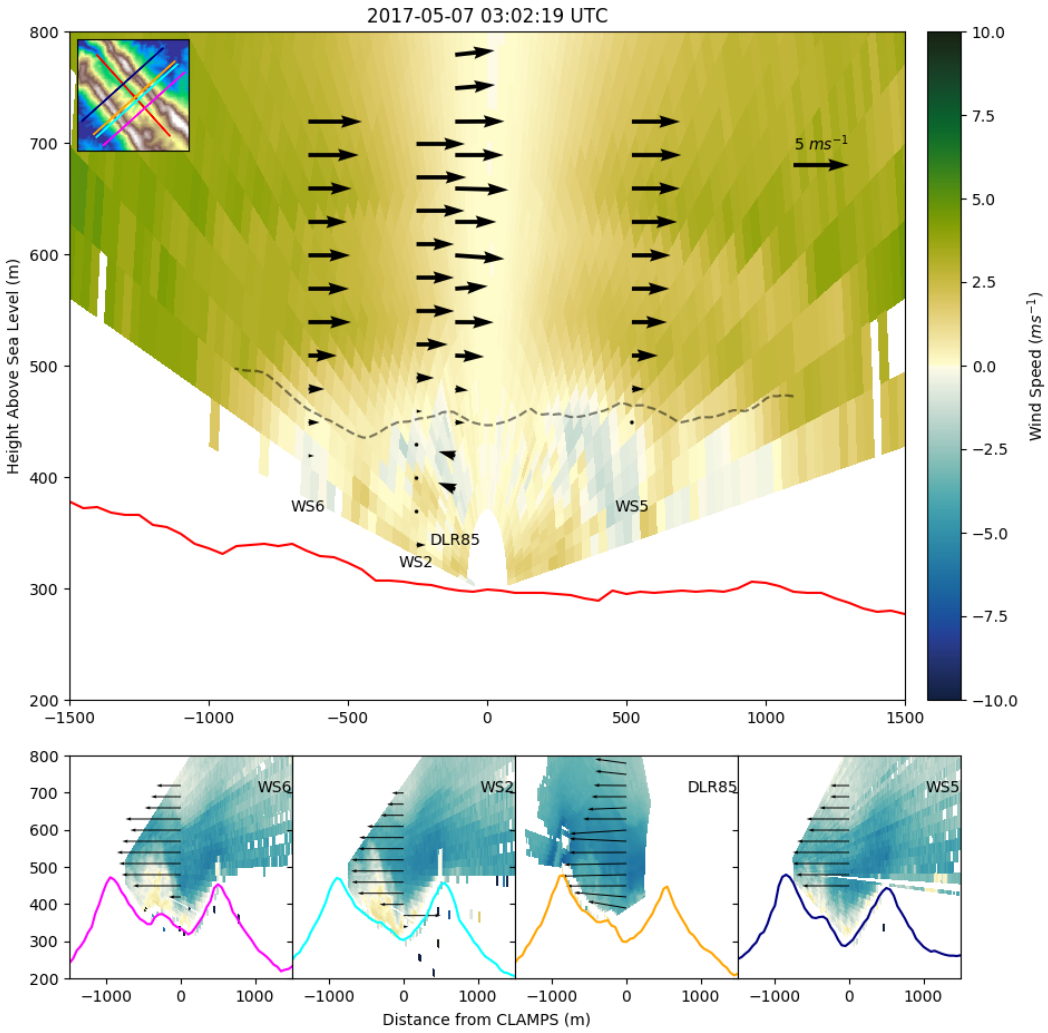

Figure 4.6: Top: Along valley cross section of the flow from the early morning of May 7th at 03 UTC. The color fill is the LOS velocity projected into the horizontal from the OU RHI used to create the virtual towers. Positive values indicate flow in the +X direction, which is directed to the NW. The overlaid vectors are the components of the virtual towers projected into the plane of the RHI scan. The inset plot shows how the terrain cross sections are oriented. The dashed line indicates the ridge top and the solid lines correspond to the terrain cross section from the inset plot. Bottom row: Similar to the top row, only in the cross valley sense. +X here points to the NE.

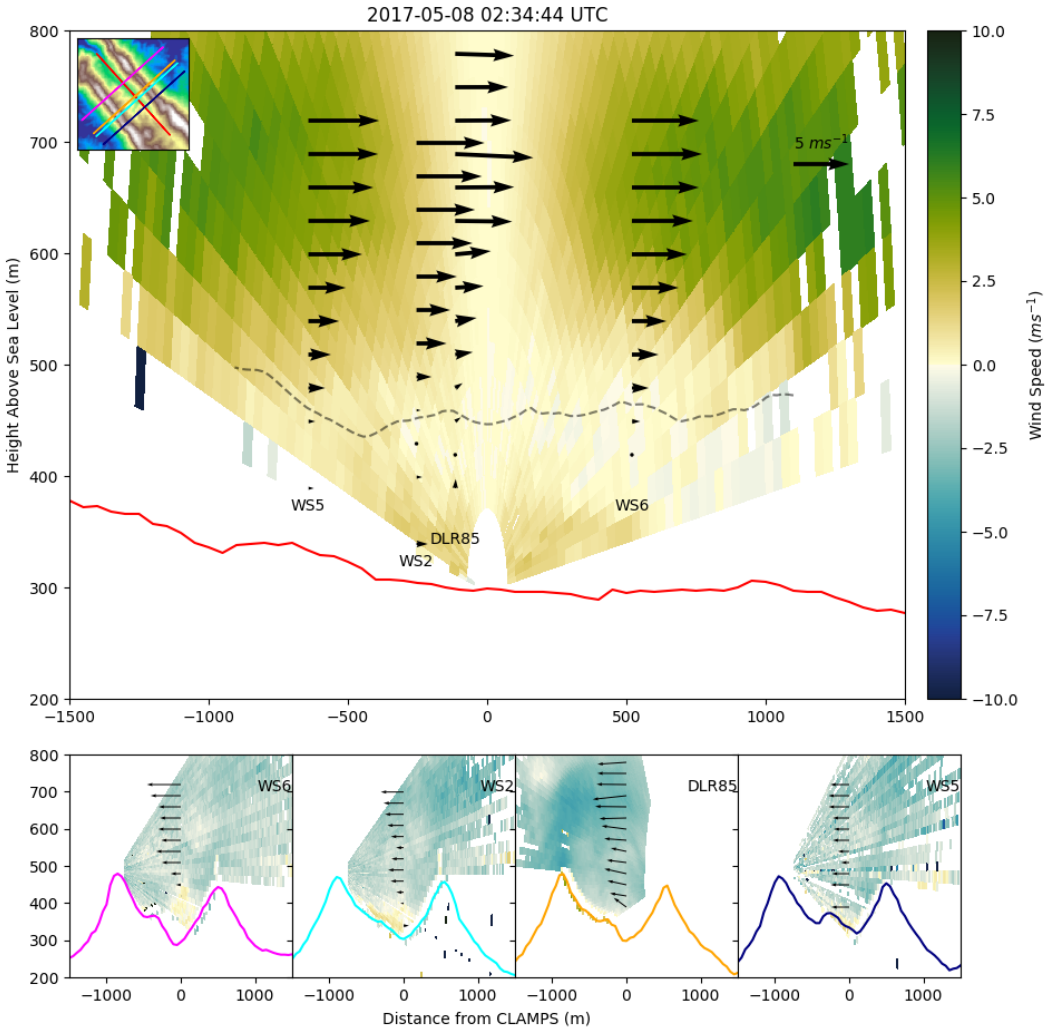

Figure 4.7: Same as Figure 4.6, but for the morning of May 8th around 0230 UTC.

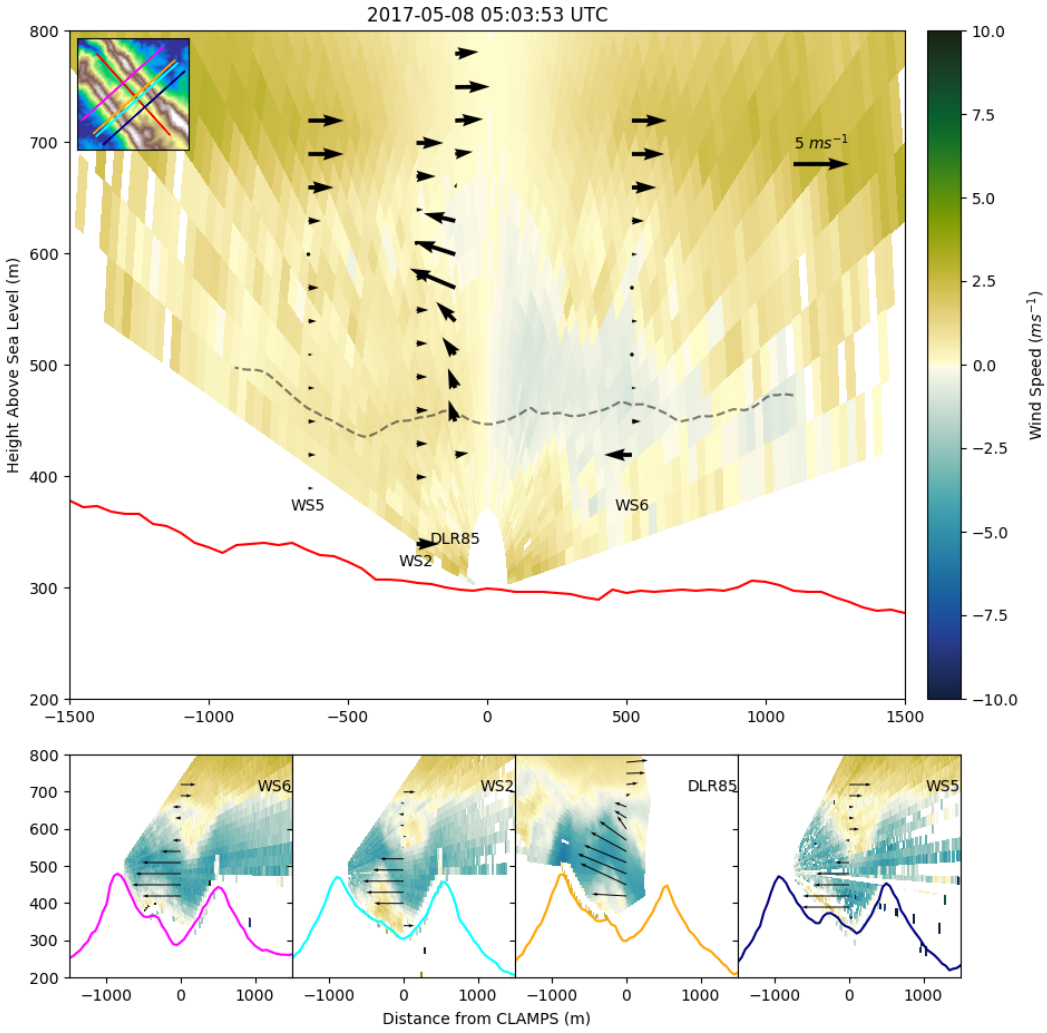

Figure 4.8: Same as Figure 4.6, but for the morning of May 8th around 05 UTC.

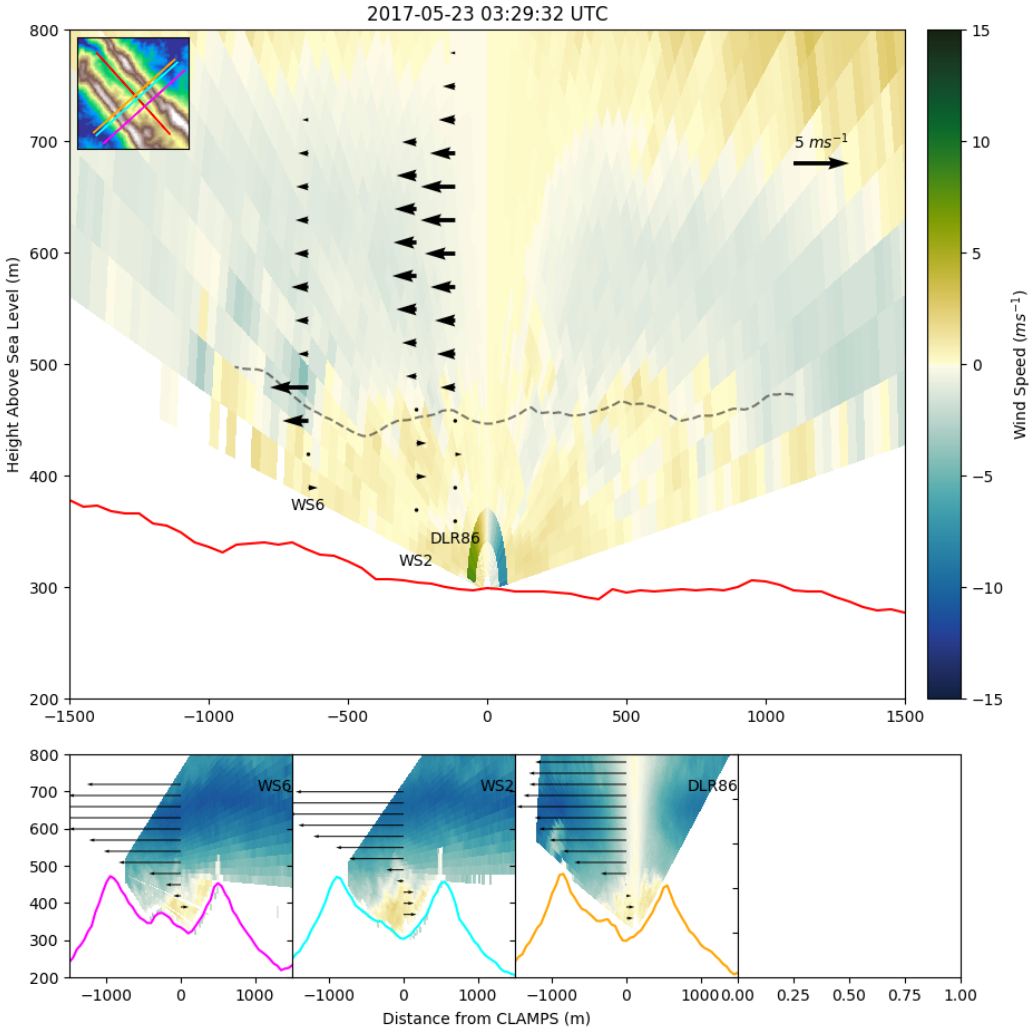

Figure 4.9: Same as Figure 4.6, but for May 23rd. Additionally, plot on the bottom are all 2D retrievals because DLR85 was not operating correctly. WS5 is missing for the same reason.

Chapter 5

Concluding Remarks and Future Work

Complex terrain and its implication on the wind energy sector is a quickly growing area of research. With the availability of DLs and other remote sensing platforms, scientists are now able to gain insights into flows that were not possible before.

Recent field experiments have sought to further the understanding of flows in mountainous terrain (e.g. MATERHORN, T-REX), but these flows are still on a rather large scale. The terrain in Perdigão provided a unique opportunity to study flows on a smaller scale, one more applicable to the wind energy sector. At the time this thesis was written, data from all the different participants are still being quality controlled and understood. With the number of instruments in this terrain, it will take years to synthesize all the different datasets into coherent conclusions.

5.1 Conclusions

The climatological winds observed during the campaign agreed relatively well with the climatology that was performed before the IOP. This study took it one step further and looked at differences between nocturnal and daytime winds and found there is a distinct difference in the winds at those times. Winds at the top of the ridge (and even higher) are clearly impacted by the battle between the synoptic flow and the regional thermal flows given their NE/SW preference.

In general, the most stable nights inside the valley were characterized by winds from the NE after 00 UTC. Interestingly, winds during these nights often was from the NW during the early evening transition before veering to the NE after 00 UTC. This again lends credit to the presence of some sort of regional circulation due to the diurnal cycle. Since the winds overnight were nearly always perpendicular to the ridges, many phenomena were consistently observed including gravity waves, valley flows, recirculations, and low-level jets.

Utilizing multi-Doppler retrievals can effectively augment more traditional observations, like meteorological towers. The virtual towers revealed that recirculations are not consistently present in all parts of the valley. This causes flow to be heterogeneous along the length of the valley. For example, on May 8th, 2017 the flow in the valley in regions with a strong recirculation was often slower than flow that did not encounter a recirculation. Additionally, these virtual towers are able to retrieve winds in areas where methods like the VAD or DBS scans rely on assumptions that are not necessarily valid.

5.2 Future Work

The analyses presented here only scratch the surface of the dataset collected in Perdigão. As more datasets are quality controlled (or produced in the case of virtual towers), more insight can be gained into the flows.

One important dataset that is still needed is thermodynamic profiles of the approach and exit flow. Though the CLAMPS MWR was located inside the valley, there were two more MWRs placed outside (one from DLR and one from Notre Dame) of the valley to collect these profiles. However, as of now, the retrievals from all the different MWRs use different retrieval methods and there was no bias correction performed before running the retrieval. To remedy this, all the MWR data will be run using MWRoe and utilize the same bias correction method used

for the CLAMPS MWR. This way, all the retrievals will be consistent (whether good or bad).

Additionally, in the days following the end of the IOP, a side-by-side comparison of the MWRs was performed at the Lower Orange site near the CLAMPS MWR. Using these data, differences between the MWR models can be teased out. Additionally, retrievals from this time can be compared to the collocated AERI and water vapor Differential Absorption Lidar.

One final thing that needs to be done with the OU MWR data specifically is to include the off-zenith scans into the retrieval. Due to time constraints, they were not initially included in the retrieval. Doing so should help to improve the retrievals in the lower levels.

Improvements to the OU DL processing and quality assurance are actively being worked on, specifically with regard to vertical velocity variance estimates using the Lenschow et al. (2000) method and the more in depth work done by Bonin et al. (2016).

With respect to Section 3.1, more work needs to be done to identify patterns in the thermodynamic data observed by CLAMPS. For example, patterns could become apparent by analyzing the Richardson or Fronde number of the flow. However, the approach flow will be the most important part, so trustworthy thermodynamic profiles from the MWR are necessary before this can proceed.

Bibliography

Arya, P. S., 2001: *Introduction to Micrometeorology*, Vol. 79. Academic Press.

Ayotte, K. W. and D. E. Hughes, 2004: Observations of boundary-layer wind-tunnel flow over isolated ridges of varying steepness and roughness. *Boundary-Layer Meteorology*, **112 (3)**, 525–556, doi:10.1023/B:BOUN.0000030663.13477.51, URL https://doi.org/10.1023/B:BOUN.0000030663.13477.51.

Banta, R. M., Y. L. Pichugina, N. D. Kelley, R. M. Hardesty, and W. A. Brewer, 2013: Wind energy meteorology: Insight into wind properties in the turbine-rotor layer of the atmosphere from high-resolution doppler lidar. *Bulletin of the American Meteorological Society*, **94 (6)**, 883–902, doi:10.1175/BAMS-D-11-00057.1.

Banta, R. M., et al., 2015: 3d volumetric analysis of wind turbine wake properties in the atmosphere using high-resolution doppler lidar. *Journal of Atmospheric and Oceanic Technology*, **32 (5)**, 904–914, doi:10.1175/JTECH-D-14-00078.1, URL https://doi.org/10.1175/JTECH-D-14-00078.1.

Beljaars, A. C. M., J. L. Walmsley, and P. A. Taylor, 1987: A mixed spectral finite-difference model for neutrally stratified boundary-layer flow over roughness changes and topography. *Boundary-Layer Meteorology*, **38 (3)**, 273–303, doi:10.1007/BF00122448, URL https://doi.org/10.1007/BF00122448.

Bingöl, F., J. Mann, and D. Foussekis, 2009: Conically scanning lidar error in complex terrain. *Meteorologische Zeitschrift*, **18 (2)**, 189–195, doi:10.1127/0941-2948/2009/0368, URL http://dx.doi.org/10.1127/0941-2948/2009/0368.

Blumberg, W. G., D. D. Turner, U. Löhnert, and S. Castleberry, 2015: Ground-based temperature and humidity profiling using spectral infrared and microwave observations. part ii: Actual retrieval performance in clear-sky and cloudy conditions. *Journal of Applied Meteorology and Climatology*, **54 (11)**, 2305–2319, doi:10.1175/JAMC-D-15-0005.1.

Bonin, T. A., J. F. Newman, P. M. Klein, P. B. Chilson, and S. Wharton, 2016: Improvement of vertical velocity statistics measured by a doppler lidar

through comparison with sonic anemometer observations. *Atmospheric Measurement Techniques*, **9 (12)**, 5833–5852, doi:10.5194/amt-9-5833-2016, URL https://www.atmos-meas-tech.net/9/5833/2016/.

Bradley, E. F., 1968: A micrometeorological study of velocity profiles and surface drag in the region modified by a change in surface roughness. *Quarterly Journal of the Royal Meteorological Society*, **94 (401)**, 361–379, doi:10.1002/qj.49709440111.

Bradley, E. F., 1980: An experimental study of the profiles of wind speed, shearing stress and turbulence at the crest of a large hill. *Quarterly Journal of the Royal Meteorological Society*, **106 (447)**, 101–123, doi:10.1002/qj.49710644708.

Bradley, S., A. Strehz, and S. Emeis, 2015: Remote sensing winds in complex terrain? a review. *Meteorologische Zeitschrift*, **24 (6)**, 547–555, doi:10.1127/metz/2015/0640, URL http://dx.doi.org/10.1127/metz/2015/0640.

Britter, R. E., J. C. R. Hunt, and K. J. Richards, 1981: Air flow over a two-dimensional hill: Studies of velocity speed-up, roughness effects and turbulence. *Quarterly Journal of the Royal Meteorological Society*, **107 (451)**, 91–110, doi:10.1002/qj.49710745106.

Browning, K. A. and R. Wexler, 1968: The determination of kinematic properties of a wind field using doppler radar. *Journal of Applied Meteorology*, **7 (1)**, 105–113, doi:10.1175/1520-0450(1968)007⟨0105:TDOKPO⟩2.0.CO;2.

Calaf, M., C. Meneveau, and J. Meyers, 2010: Large eddy simulation study of fully developed wind-turbine array boundary layers. *Physics of Fluids*, **22 (1)**, 015 110, doi:10.1063/1.3291077, URL https://doi.org/10.1063/1.3291077, https://doi.org/10.1063/1.3291077.

Calaf, M., M. B. Parlange, and C. Meneveau, 2011: Large eddy simulation study of scalar transport in fully developed wind-turbine array boundary layers. *Physics of Fluids*, **23 (12)**, 126 603, doi:10.1063/1.3663376, URL https://doi.org/10.1063/1.3663376, https://doi.org/10.1063/1.3663376.

Calhoun, R., R. Heap, M. Princevac, R. Newsom, H. Fernando, and D. Ligon, 2006: Virtual towers using coherent doppler lidar during the joint urban 2003 dispersion experiment. *Journal of Applied Meteorology and Climatology*, **45 (8)**, 1116–1126, doi:10.1175/JAM2391.1, URL https://doi.org/10.1175/JAM2391.1.

Choukulkar, A., et al., 2017: Evaluation of single and multiple doppler lidar techniques to measure complex flow during the xpia field campaign. *Atmospheric Measurement Techniques*, **10 (1)**, 247–264, doi:10.5194/amt-10-247-2017, URL https://www.atmos-meas-tech.net/10/247/2017/.

Claussen, M., 1988: On the inner-layer scale height of boundary-layer flow over low hills. *Boundary-Layer Meteorology*, **44 (4)**, 411–413, doi:10.1007/BF00123025, URL https://doi.org/10.1007/BF00123025.

Damian, T., A. Wieser, K. Träumner, U. Corsmeier, and C. Kottmeier, 2014: Nocturnal low-level jet evolution in a broad valley observed by dual doppler lidar. *Meteorologische Zeitschrift*, **23 (3)**, 305–313, doi:DOI10.1127/0941-2948/2014/0543.

Deardorff, J. W., 1972: Numerical investigation of neutral and unstable planetary boundary layers. *Journal of the Atmospheric Sciences*, **29 (1)**, 91–115, doi:10.1175/1520-0469(1972)029⟨0091:NIONAU⟩2.0.CO;2.

Deardorff, J. W., 1974: Three-dimensional numerical study of the height and mean structure of a heated planetary boundary layer. *Boundary Layer Meteorology*, **7 (1)**, doi:10.1007/BF00224974.

Debnath, M., et al., 2017: Assessment of virtual towers performed with scanning wind lidars and ka-band radars during the xpia experiment. *Atmospheric Measurement Techniques*, **10 (3)**, 1215–1227, doi:10.5194/amt-10-1215-2017, URL https://www.atmos-meas-tech.net/10/1215/2017/.

Drechsel, S., G. J. Mayr, M. Chong, M. Weissmann, A. Dörnbrack, and R. Calhoun, 2009: Three-dimensional wind retrieval: Application of muscat to dual-doppler lidar. *Journal of Atmospheric and Oceanic Technology*, **26 (3)**, 635–646, doi:10.1175/2008JTECHA1115.1, URL https://doi.org/10.1175/2008JTECHA1115.1.

Egger, J., 1985: Slope winds and the axisymmetric circulation over antarctica. *Journal of the Atmospheric Sciences*, **42 (17)**, 1859–1867, doi:10.1175/1520-0469(1985)042⟨1859:SWATAC⟩2.0.CO;2.

Elliott, W. P., 1958: The growth of the atmospheric internal boundary layer. *Eos, Transactions American Geophysical Union*, **39 (6)**, 1048–1054, doi:10.1029/TR039i006p01048.

Fernando, H., 2010: Fluid dynamics of urban atmospheres in complex terrain. *Annual Review of Fluid Mechanics*, **42 (1)**, 365–389, doi:10.1146/annurev-fluid-121108-145459.

Fernando, H. J. S., et al., 2015: The materhorn: Unraveling the intricacies of mountain weather. *Bulletin of the American Meteorological Society*, **96 (11)**, 1945–1967, doi:10.1175/BAMS-D-13-00131.1, URL https://doi.org/10.1175/BAMS-D-13-00131.1.

Grachev, A. A., L. S. Leo, S. D. Sabatino, H. J. S. Fernando, E. R. Pardyjak, and C. W. Fairall, 2016: Structure of turbulence in katabatic flows below and above the wind-speed maximum. *Boundary-Layer Meteorology*, **159 (3)**, 469–494.

Grubišić, V., et al., 2008: The terrain-induced rotor experiment. *Bulletin of the American Meteorological Society*, **89 (10)**, 1513–1534, doi:10.1175/2008BAMS2487.1.

Hill, M., R. Calhoun, H. J. S. Fernando, A. Wieser, A. Dörnbrack, M. Weissmann, G. Mayr, and R. Newsom, 2010: Coplanar doppler lidar retrieval of rotors from t-rex. *Journal of the Atmospheric Sciences*, **67 (3)**, 713–729, doi:10.1175/2009JAS3016.1, URL `https://doi.org/10.1175/2009JAS3016.1`.

Hunt, J. C. R., 1971: A theory for the laminar wake of a two-dimensional body in a boundary layer. *Journal of Fluid Mechanics*, **49 (1)**, 159–178, doi:10.1017/S0022112071001988.

Hunt, J. C. R., S. Leibovich, and K. J. Richards, 1988: Turbulent shear flows over low hills. *Quarterly Journal of the Royal Meteorological Society*, **114 (484)**, 1435–1470, doi:10.1002/qj.49711448405.

Jackson, P. S. and J. C. R. Hunt, 1975: Turbulent wind flow over a low hill. *Quarterly Journal of the Royal Meteorological Society*, **101 (430)**, 929–955, doi:10.1002/qj.49710143015.

Jensen, D. D., D. F. Nadeau, S. W. Hoch, and E. R. Pardyjak, 2016: Observations of near-surface heat-flux and temperature profiles through the early evening transition over contrasting surfaces. *Boundary-Layer Meteorology*, **159 (3)**, 567–587.

Jensen, N. O., E. Lundtang Petersen, and I. Troen, 1984: *Extrapolation of Mean Wind Statistics with Special Regard to Wind Energy Applications. WMO. World Climate Programme Report No. WCP-86*. World Meteorological Organization.

Kim, H. G. and V. C. Patel, 2000: Test of turbulence models for wind flow over terrain with separation and recirculation. *Boundary-Layer Meteorology*, **94 (1)**, 5–21, doi:10.1023/A:1002450414410, URL `https://doi.org/10.1023/A:1002450414410`.

Klein, P., et al., 2015: Lable: A multi-institutional, student-led, atmospheric boundary layer experiment. *Bulletin of the American Meteorological Society*, **96 (10)**, 1743–1764, doi:10.1175/BAMS-D-13-00267.1, URL `https://doi.org/10.1175/BAMS-D-13-00267.1`.

Knuteson, R. O., et al., 2004a: Atmospheric emitted radiance interferometer. part i: Instrument design. *Journal of Atmospheric and Oceanic Technology*, **21 (12)**, 1763–1776, doi:10.1175/JTECH-1662.1, URL `https://doi.org/10.1175/JTECH-1662.1`.

Knuteson, R. O., et al., 2004b: Atmospheric emitted radiance interferometer. part ii: Instrument performance. *Journal of Atmospheric and Oceanic Technology*,

21 (12), 1777–1789, doi:10.1175/JTECH-1663.1, URL https://doi.org/10.1175/JTECH-1663.1.

Kutzbach, J., 1961: Investigations of the modifications of wind profiles by artificially controlled surface roughness. University of Wisconsin, 71-114 pp.

Lenschow, D. H., V. Wulfmeyer, and C. Senff, 2000: Measuring second- through fourth-order moments in noisy data. *Journal of Atmospheric and Oceanic Technology*, **17 (10)**, 1330–1347, doi:10.1175/1520-0426(2000)017⟨1330:MSTFOM⟩2.0.CO;2.

Leo, L. S., M. Y. Thompson, S. Di Sabatino, and H. J. S. Fernando, 2016: Stratified flow past a hill: Dividing streamline concept revisited. *Boundary-Layer Meteorology*, **159 (3)**, 611–634, doi:10.1007/s10546-015-0101-1, URL https://doi.org/10.1007/s10546-015-0101-1.

Mann, J., et al., 2017: Complex terrain experiments in the new european wind atlas. *Philosophical Transactions of the Royal Society of London A: Mathematical, Physical and Engineering Sciences*, **375 (2091)**, doi:10.1098/rsta.2016.0101, URL http://rsta.royalsocietypublishing.org/content/375/2091/20160101, http://rsta.royalsocietypublishing.org/content/375/2091/20160101.full.pdf.

Mason, P. J. and J. C. King, 1985: Measurements and predictions of flow and turbulence over an isolated hill of moderate slope. *Quarterly Journal of the Royal Meteorological Society*, **111 (468)**, 617–640, doi:10.1002/qj.49711146818.

Mason, P. J. and R. I. Sykes, 1979: Flow over an isolated hill of moderate slope. *Quarterly Journal of the Royal Meteorological Society*, **105 (444)**, 383–395, doi:10.1002/qj.49710544405.

Menke, R., N. Vasiljević, K. Hansen, A. N. Hahmann, and J. Mann, 2018: Does the wind turbine wake follow the topography? – a multi-lidar study in complex terrain. *Wind Energy Science Discussions*, **2018**, 1–18, doi:10.5194/wes-2018-21, URL https://www.wind-energ-sci-discuss.net/wes-2018-21/.

Mickle, R. E., N. J. Cook, A. M. Hoff, N. O. Jensen, J. R. Salmon, P. A. Taylor, G. Tetzlaff, and H. W. Teunissen, 1988: The askervein hill project: Vertical profiles of wind and turbulence. *Boundary-Layer Meteorology*, **43 (1)**, 143–169.

Monin, A. and A. Obukhov, 1959: Basic laws of turbulent mixing in the ground layer of the atmosphere.

Newman, J. F., T. A. Bonin, P. M. Klein, S. Wharton, and R. K. Newsom, 2016: 3d volumetric analysis of wind turbine wake properties in the atmosphere using high-resolution doppler lidar. *Wind Energy*, **19 (2)**, 2239, 2254, doi:https://doi.org/10.1002/we.1978.

Panofsky, H. A. and A. A. Townsend, 1964: Change of terrain roughness and the wind profile. *Quarterly Journal of the Royal Meteorological Society*, **90 (384)**, 147–155, doi:10.1002/qj.49709038404.

Päschke, E., R. Leinweber, and V. Lehmann, 2015: An assessment of the performance of a 1.5 μmdoppler lidar for operational vertical wind profiling based on a 1-year trial. *Atmospheric Measurement Techniques*, **8 (6)**, 2251–2266, doi:10.5194/amt-8-2251-2015, URL `https://www.atmos-meas-tech.net/8/2251/2015/`.

Prandtl, L., 1942: Fuhrer durch die stromungslehre.

Putnam, P. C., 1948: *Power from the wind*. New York: Van Nostrand Reinhold.

Queney, P., 1948: The problem of air flow over mountains: A summary of theoretical studies. *Bulletin of the American Meteorological Society*, **29 (1)**, 16–26, URL `http://www.jstor.org/stable/26257649`.

Rose, T., S. Crewell, U. Löhnert, and C. Simmer, 2005: A network suitable microwave radiometer for operational monitoring of the cloudy atmosphere. *Atmospheric Research*, **75 (3)**, 183, 200, doi:https://doi.org/10.1002/we.1978.

Sawyer, J. S., 1962: Gravity waves in the atmosphere as a three-dimensional problem. *Quarterly Journal of the Royal Meteorological Society*, **88 (378)**, 412–425, doi:10.1002/qj.49708837805, URL `https://rmets.onlinelibrary.wiley.com/doi/abs/10.1002/qj.49708837805`, `https://rmets.onlinelibrary.wiley.com/doi/pdf/10.1002/qj.49708837805`.

Scorer, R. S., 1949: Theory of waves in the lee of mountains. *Quarterly Journal of the Royal Meteorological Society*, **75 (323)**, 41–56, doi:10.1002/qj.49707532308.

Scorer, R. S. and M. Wilkinson, 1956: Waves in the lee of an isolated hill. *Quarterly Journal of the Royal Meteorological Society*, **82 (354)**, 419–427, doi:10.1002/qj.49708235405.

Shapiro, A. and E. Fedorovich, 2007: Katabatic flow along a differentially cooled sloping surface. *Journal of Fluid Mechanics*.

Shapiro, A. and E. Fedorovich, 2008: Coriolis effects in homogeneous and inhomogeneous katabatic flows. *Quarterly Journal of the Royal Meteorological Society*, doi:10.1002/qj.217.

Sheppard, P. A., 1956: Airflow over mountains. *Quarterly Journal of the Royal Meteorological Society*, **82 (354)**, 528–529, doi:10.1002/qj.49708235418, URL `https://rmets.onlinelibrary.wiley.com/doi/abs/10.1002/qj.49708235418`, `https://rmets.onlinelibrary.wiley.com/doi/pdf/10.1002/qj.49708235418`.

Smith, F. T., 1973: Laminar flow over a small hump on a flat plate. *Journal of Fluid Mechanics*, **57 (4)**, 803–824, doi:10.1017/S002211207300203X.

Snyder, W. H., R. S. Thompson, R. E. Eskridge, R. E. Lawson, I. P. Castro, J. T. Lee, J. C. R. Hunt, and Y. Ogawa, 1985: The structure of strongly stratified flow over hills: dividing-streamline concept. *Journal of Fluid Mechanics*, **152**, 249–288, doi:10.1017/S0022112085000684.

Stearns, C. R., 1964: Wind-profile modification experiments using fields of christmas trees on the ice of lake mendota. University of Wisconsin, Department of Meteorology, 59 pp.

Strauch, R. G., D. A. Merritt, K. P. Moran, K. B. Earnshaw, and D. V. D. Kamp, 1984: The colorado wind-profiling network. *Journal of Atmospheric and Oceanic Technology*, **1 (1)**, 37–49, doi:10.1175/1520-0426(1984)001⟨0037:TCWPN⟩2.0.CO;2.

Sykes, R. I., 1980: An asymptotic theory of incompressible turbulent boundary-layer flow over a small hump. *Journal of Fluid Mechanics*, **101 (3)**, 647–670, doi:10.1017/S002211208000184X.

Taylor, P. A., P. J. Mason, and E. F. Bradley, 1987: Boundary-layer flow over low hills. *Boundary-Layer Meteorology*, **39 (1)**, 107–132, doi:10.1007/BF00121870, URL `https://doi.org/10.1007/BF00121870`.

Taylor, P. A. and H. W. Teunissen, 1987: The askervein hill project: Overview and background data. *Boundary-Layer Meteorology*, **39 (1)**, 15–39, doi:10.1007/BF00121863, URL `https://doi.org/10.1007/BF00121863`.

Taylor, R. J., 1962: Small-scale advection and the neutral wind profile. *Journal of Fluid Mechanics*, **13 (4)**, 529–539, doi:10.1017/S0022112062000919.

Teunissen, H. W., M. E. Shokr, A. J. Bowen, C. J. Wood, and D. W. R. Green, 1987: The Askervein Hill Project: Wind-tunnel simulations at three length scales. *Boundary-Layer Meteorology*, **40**, 1–29, doi:10.1007/BF00140067.

Turner, D. D. and U. Löhnert, 2014: Information content and uncertainties in thermodynamic profiles and liquid cloud properties retrieved from the ground-based atmospheric emitted radiance interferometer (aeri). *Journal of Applied Meteorology and Climatology*, **53 (3)**, 752–771, doi:10.1175/JAMC-D-13-0126.1, URL `https://doi.org/10.1175/JAMC-D-13-0126.1`, `https://doi.org/10.1175/JAMC-D-13-0126.1`.

Vasiljević, N., et al., 2017: Perdigão 2015: methodology for atmospheric multi-doppler lidar experiments. *Atmospheric Measurement Techniques*, **10 (9)**, 3463–3483, doi:10.5194/amt-10-3463-2017, URL `https://www.atmos-meas-tech.net/10/3463/2017/`.

Waldteufel, P. and H. Corbin, 1979: On the analysis of single-doppler radar data. *Journal of Applied Meteorology*, **18 (4)**, 532–542, doi:10.1175/1520-0450(1979)018⟨0532:OTAOSD⟩2.0.CO;2, URL https://doi.org/10.1175/1520-0450(1979)018<0532:OTAOSD>2.0.CO;2.

Walmsley, J. L., P. A. Taylor, and T. Keith, 1986: A simple model of neutrally stratified boundary-layer flow over complex terrain with surface roughness modulations (ms3djh/3r). *Boundary-Layer Meteorology*, **36 (1)**, 157–186, doi:10.1007/BF00117466, URL https://doi.org/10.1007/BF00117466.

Wang, H., R. J. Barthelmie, A. Clifton, and S. C. Pryor, 2015: Wind measurements from arc scans with doppler wind lidar. *Journal of Atmospheric and Oceanic Technology*, **32 (11)**, 2024–2040, doi:10.1175/JTECH-D-14-00059.1.

Weissmann, M., A. Dörnbrack, and J. D. Doyle, 2009: Vorticity from line-of-sight lidar velocity scans. *Journal of Atmospheric and Oceanic Technology*, **26 (12)**, 2683–2690, doi:10.1175/2009JTECHA1260.1, URL https://doi.org/10.1175/2009JTECHA1260.1.

Willis, G. E. and J. W. Deardorff, 1974: A laboratory model of the unstable planetary boundary layer. *Journal of the Atmospheric Sciences*, **31 (5)**, 1297–1307, doi:10.1175/1520-0469(1974)031⟨1297:ALMOTU⟩2.0.CO;2.

Wood, N., 1995: The onset of separation in neutral, turbulent flow over hills. *Boundary-Layer Meteorology*, **76 (1)**, 137–164, doi:10.1007/BF00710894, URL https://doi.org/10.1007/BF00710894.

Wood, N., 2000: Wind flow over complex terrain: A historical perspective and the prospect for large-eddy modelling. *Boundary-Layer Meteorology*, **96 (1)**, 11–32, doi:10.1023/A:1002017732694, URL https://doi.org/10.1023/A:1002017732694.